DIFFERENT STATES AND DIFFERENT POPULATIONS OF NEURAL STEM CELLS IN THE ADULT HIPPOCAMPUS

by

Ryan Stadel

A dissertation submitted to Johns Hopkins University in conformity with the requirements for the degree of Doctor of Philosophy

Baltimore, Maryland

March, 2015

Abstract

Over the past couple of decades, a central dogma in neuroscience has been overturned, the belief that no new neurons are generated in the adult mammalian brain. It has now been shown that within discrete regions there is generation and incorporation of new neurons in the adult brain, including humans. The origins of these newborn cells as well as whether a bona fide adult neural stem cell exists is, however, under intense debate.

Hallmark properties of individual stem cells include repeated self-renewal and the potential of differentiation into specialized cells. Complex stem cell behavior, however, has led to uncertainty regarding their identities, basic characteristics and relationships in multiple somatic tissues. Recent development of clonal lineage-tracing of individual cells has revealed a population of quiescent radial glia-like neural stem cells (RGLs) marked by *Nestin-CreER*^{T2} (Nestin$^{\#}$) in the adult mouse hippocampus. Whether Nestin$^{\#}$ RGLs represent the only, homogeneous population of stem cells in the adult SGZ remains unclear. In my thesis, we performed clonal lineage-tracing of RGLs marked by *Gli1-CreER*^{T2} (Gli1$^{\#}$) and *Ascl1-CreER*^{T2} (Ascl1$^{\#}$). Both RGLs exhibit stem cell characteristics, but differ in their self-renewal modes and cell cycle properties. Time-course and computational analyses suggest that Gli1$^{\#}$ marks the stochastic, multipotent Nestin$^{\#}$-RGL population in a pre-activation state, whereas Ascl1$^{\#}$-RGLs represent a distinct, neuronal fate biased population. Furthermore, Gli1$^{\#}$-RGLs and Nestin$^{\#}$-RGLs acquire Ascl1$^{\#}$-RGL-like properties upon injury. My study resolves dynamic behavior of apparent similar stem cells into different states of the same population and discrete populations that co-exist in the same tissue.

Thesis Advisor: Hongjun Song, Ph.D., Professor of Neurology and Neuroscience

Reader: Guo-li Ming, Ph.D., Professor of Neurology, Neuroscience, Psychiatry and behavioral Sciences

Preface

I'd like to firstly thank my thesis advisor Dr. Hongjun Song for his support throughout my graduate work. Not only did he personally guide me through various writings and presentations but through example, I've learned what it takes to be an excellent scientist.

In addition I'd like to thank my thesis committee, including Dr. David Valle, Dr. Guo-li Ming, Dr. Randall Reed, and Dr. Duo-jia Pan. Their advice and guidance have helped shape the completion of my thesis work. Dr. Song's laboratory, which works jointly with Dr. Ming's laboratory, was a wonderful place to work and learn. I'd like to offer my gratitude to current and past members of the Song/Ming laboratories. I'd especially like to thank Dr. Michael Bonaguidi, who initiated and guided me through my thesis work and much of the work presented was done in equal collaboration. I'd also like to personally thank the contributions of Dr. Gerald Sun and Yi Zhou (Joey). My thanks also go out to my collaborators at Cambridge, Dr. Benjamin Simons and Theresa Krieger, who performed much of the computational analysis included in my thesis.

My thanks go out to the entire JHMI Human Genetics Graduate Program and it was an honor to be a part of such a wonderful and prestigious program. The director Dr. David Valle's support and guidance was invaluable as was the administrator, Sandy Muscelli. Without Sandy's step by step instruction, completion of this thesis would not have been possible. Importantly, I've made invaluable and life-long friends from my classmates.

I would of course like to thank all my friends. I'd especially like to mention Mark who has always been there for me since childhood. Additional thanks go out to Sebastian, a special person who greatly enriches my life.

Lastly I'd like to thank my family. Thank you to my brother and his family and to my niece and new nephew. My grandparents have always told me how proud they were of me, but it’s me who is proud and lucky to have them in my life. Lastly, my parents have been inspirational and have always offered their love and support. All I am including this thesis is dedicated to them.

Contents

List of Tables

List of Figures

Abbreviations

Ascl1$^{\#}$: Ascl1::CreERT2 lineage traced;

BrdU: bromodeoxyuridine

dpi: days post induction;

GFP: green fluorescent protein;

Gli1$^{\#}$: Gli1::CreERT2 lineage traced;

IN: immature neuron;

IPC: intermediate progenitor cell;

nIPC: neuronal intermediate progenitor cell;

mT/mG: membrane bound tomato/membrane bound GFP;

MN: mature neuron;

NB: neuroblast;

OPC: oligodendrocyte progenitor cell;

P_{RA}: probability of a RGL astrocytic division;

P_{RR}: probability of an RGL-RGL symmetric division;

P_{RN}: probability of an RGL neuronal division;

nIPC: neural intermediate progenitor cell;

Nestin$^{\#}$: Nestin::CreERT2 lineage traced;

RGL: radial-glia like;

SGZ: subgranular zone;

SVZ: subventricular zone;

T_{entry}: time until first RGL division;

T_c: time until RGL cell cycle re-entry;

YFP: yellow fluorescent protein;

Z/EG: lacZ/enhanced GFP;

1 Introduction

1.1 Adult precursor cells

Adult precursor cells contribute to ongoing tissue maintenance and repair after injury[1-5]. Stem cells are defined by the capacity to self-renew without differentiating for a prolonged period of time, and these properties distinguish stem cells from other more committed progenitor cells, which more readily differentiate into specific cell types. Stem and progenitor cells (collectively called precursor cells) are further classified by the diversity of their progeny. Individual stem cells can give rise to one (unipotential, such as spermatagonial stem cells) or many lineages (multipotential, such as hematopoietic stem cells) and their division mode may be constitutively biased or stochastic [6]. Complicating findings, evidence points to the possibility that multiple precursors co-exist and exhibit different stem cell properties[7]. One common theme across most, but not all, somatic stem cell compartments is the presence of these multiple precursors where one maintains everyday tissue homeostasis, while another precursor is activated and becomes available upon injury[8]. These concepts have led to the concept of cell lineages arranged in a hierarchy where the precursor cell with the largest capacity is at the top layer and the most differentiated cells are located at the bottom[9]. For example, a multipotent stem cell could represent the top hierarchal layer, which could generate a more committed unipotent stem or progenitor cell, which in turn generate a fully differentiated cell. Confounding hierarchies, evidence suggests certain cells may gain capacity upon injury such as ependymal cells in the adult brain[10-12] or epithelial cells upon injury[13], and this gain of capacity with injury is even proposed in tissues not traditionally thought to divide such as the heart or lung[14, 15].

Conversely some tissues contain classic adult precursor cell compartments where precursors divide due to high cell turnover or demand and include the epidermis (skin, hair-follicle, and sweat gland), intestine, hematopoietic and germline (ovary and testes)[16]. Emerging evidence over the last couple decades, has added two discrete areas of the adult brain to this list, the subgranular zone of the hippocampus (SGZ) and the subventricular zone of the lateral ventricle (SVZ)[17]. Unlike the functional turnover present in many classic adult precursor cell compartments, in the brain, studies have started to elucidate that new neurons may be generated for specific brain functions for example SVZ generated interneurons may contribute to olfactory functions. On the other hand, new excitatory neurons generated in the SGZ may have a function in learning, memory, and emotions[17]. Ultimately, identifying stem cells in their native environment and elucidating their basic characteristics and lineage relationships are fundamental goals toward understanding tissue homeostasis and plasticity under basal and pathological conditions, which in turn has significant implications for regenerative medicine.

1.2 Precursor cell heterogeneity

An emerging principle of precursor cell biology is the manifestation of heterogeneity within a given tissue. Apparent cell diversity may arise from differences in various precursor cell characteristics, such as proliferation dynamics, lineage bias, self-renewal capacity, or function during tissue maintenance and repair[7, 18, 19]. These complexities have resulted in substantial controversy over the identity and property of precursor cell populations in many somatic compartments, such as hematopoietic, intestinal, epithelial and neural systems[8, 20, 21]. Two major contributors to the uncertainty over precursor and stem cell identity are their highly dynamic nature and potential presence of multiple precursor types in the same tissue. For example, stem cells modify their behavior by switching between quiescent and active states. Therefore, when taken as a single snapshot, different transitory states can be observed in a single stem population and potentially mis-interpreted as different stem cell populations. Approaches designed to distinguish discrete precursor cell populations from different states of the same population would therefore provide a general framework to help resolve precursor cell heterogeneity.

Traditionally, precursor cells have been investigated at the population level via genetic fate-mapping or nucleotide analog pulsing. These approaches, while instrumental in revealing the collective potential of labeled cells, do not address properties of individual precursor cells, which could be quite heterogeneous. For example in the adult brain, population level cre-lox based fate-mapping tends to mostly take advantage of genetic labeling using a single protein marker's regulatory elements that is active in a precursor cell. Since individual neural precursors cannot be identified by any one marker, labeling of heterogeneous precursor populations results[22]. In addition to nonspecific labeling of multiple and different precursors, population studies also tend to use biased labeling methods enriching for cells within a certain state. For example, BrdU immunohistochemistry or retrovirus label actively dividing cells[22]. Even when using cre-lox based fate mapping, certain proteins such as transcription factors could be turned off and on transiently as needed therefore biasing labeling for the process or state in which this protein may be involved[22]. When focusing on the adult brain, almost all studies that provide instead clonal resolution involve removing precursor cells from their native environment such as transplant, slice culture or cell culture studies, which in addition causes high amounts of injury[22]. Therefore, higher resolution, non-biased approaches where individual precursors are studied in their native environment are needed.

1.3 Precursor cells in the adult brain

In the adult brain, emerging evidence from population studies points to the presence of multiple neural precursors (stem and progenitor cells) in the adult SGZ and SVZ with different fate biases[23-25]. These include cells traditionally thought to be progenitors, such as oligodendrocyte progenitor cells (OPCs), neuronal intermediate progenitor cells (nIPCs), as well as astrocytes upon injury[17]. Under normal conditions, the nIPCs divide, go through a stereotypic cell death[26] and mature down a developmental cascade, which include several characterized cell types[17].

On the other hand, the classic neural stem cell was originally defined retrospectively through cell culture experiments where single clones were shown to self-renew while generating neurons, astrocytes and oligodendrocytes [2, 27]. Recent reprogramming studies demonstrating the possibilities to change the cell potential in vitro have raised questions on whether cultured neural precursor cells acquire new potential not evident *in vivo*[28-30].

One proposed stem cell candidate in the SGZ, though not yet identified in the SVZ, originated through clonal retrovirus labeling using the Sox2 transcription factor[31]. These "horizontal stem cells" have a non-radial morphology similar to nIPCs and current evidence has not unambiguously distinguished this cell from an earlier stage of the nIPC lineage. Present in the SVZ but not SGZ, ependymal cells have a long history having been proposed as a possible precursor cell population. Currently, research points towards ependymal cells lacking precursor capacity basally, but may acquire capacity and produce neurons and astrocytes upon injury[10-12].

Another stem cell candidate has been confirmed through newly developed *in vivo* single cell lineage tracing, which has the capability of characterizing individual precursor cell processes and points towards the radial glia-like cell (RGL) being a true adult neural stem cell[23]. Clonal analysis via single-cell lineage-tracing in vivo provides a high resolution approach towards unraveling basic characteristics of precursor cells[1, 32]. In the nervous system, clonal lineage-tracing of largely quiescent RGLs labeled using *Nestin-CreER*^{T2} (Nestin$^{\#}$-RGL) has demonstrated the presence of self-renewing, multipotent neural stem cells within the subgranular zone (SGZ) in the adult mouse dentate gyrus [23]. One limitation of this approach, however, is the inability to predict when quiescent neural stem cells are going to activate, therefore not possible for direct observation and quantification of specific basic stem cell characteristics, such as cell cycle kinetics.

RGLs have also been discovered and traditionally called Type-B cells within the SVZ. While less clonal lineage data is available for RGLs within the SVZ, cell culture as well as very recent *in vivo* clonal analysis[33] suggests these cells may be restricted in fate as well as limited in self-renewal compared to the clonal characterization in the SGZ. Another difference between SGZ and SVZ RGLs, besides producing inhibitory versus excitatory neurons respectively, is that SVZ RGLs but not SGZ RGLs seem to produce OPCs. These along with other differences and ambiguities observed in population level studies have led to the observation of heterogeneity within the neural stem cell compartment.

1.4 Adult RGL neural stem cell heterogeneity

Heterogeneity within the SVZ includes observations of regional as well heterogeneity in stem cell fate choice. Certain studies have shown based on location certain regions of the SVZ produce different olfactory interneuron sub-types[34]. In addition, generation of astroglia seems to be spatially restricted to local migration in radial columns[35]. Also, there seems to be a dorsal versus ventral enrichment in oligodendrocyte generation[36]. Through cell culture experiments, it seem SVZ stem cells have restricted fate either producing neurons or oligodendrocytes but not both with the astrocytic fate choice shared[36]. Still many of these heterogeneity studies were done through population or cell culture studies lacking RGL specificity. Recent SVZ clonal analysis of RGLs seems to confirm the fate restriction at least within the neuronal clones as well as certain spatial restrictions when looking at newborn neurons within the olfactory bulb[33]. Still more data is needed within the SVZ to look at the clonal RGL generation of different neural cell types (astrocytes and oligodendrocytes) as well as data on the spatial locations to confirm earlier population level heterogeneity experiments.

Less has been shown regarding heterogeneity within the SGZ RGL populations. Distinct cell cycle and self-renewal properties have been suggested[23, 24, 37] and phenotypic heterogeneity exists in response to physiological changes and injury[38]. In addition, some septal versus temporal differences especially in proliferation dynamics has been noted[39-42]. Whether these observed differences reflect discrete RGL stem cell populations within the SGZ remains unknown.

To deconstruct the complexity of stem cell behavior, we developed genetic marking strategies for clonal lineage-tracing of RGLs in the adult mouse dentate gyrus using *Gli1-CreER*^{T2} [43] and *Ascl1-CreER*^{T2} [44], referred to as Gli1$^{\#}$-RGLs and Ascl1$^{\#}$-RGLs, respectively. We performed time-course experiments and computational analyses to quantify fundamental precursor

properties and systemically compared Gli1$^{\#}$-RGLs, Ascl1$^{\#}$-RGLs and previously identified Nestin$^{\#}$-RGLs. We further explored the plasticity of RGL properties upon injury. My thesis reveals the co-existence of neural stem cells with different characteristics in the adult mammalian brain and provides novel insight into endogenous somatic stem cell complexity.

2 Methods

Animals, Tamoxifen Administration and AraC Treatment

Animals were housed in a 14 hr light/10 hr dark cycle with free access to food. All procedures were performed in accordance with institutional animal guidelines. *Nestin-CreER*^{T2} mice[45], *Gli1-CreER*^{T2} [43], and *Ascl1-CreER*^{T2} [44] were used to clonally label RGLs. The following genetically modified mice were originally purchased from Jackson Labs: *Gli1-CreER*^{T2} (Strain: *Gli1*$^{tm3(cre/ERT2)Alj}$/J; stock:007913), *Z/EG*$^{f/+}$ (Strain: Tg(CAG-Bgeo/GFP)21Lbe/J; stock: 3920) [46], *Rosa-YFP*$^{f/f}$ (Strain: B6.129X1-Gt(ROSA)$^{26Sortm1(EYFP)Cos/}$J; stock: 006148), *mT/mG*$^{f/f}$ (Strain: B6.129(Cg)-*Gt(ROSA)26Sor*$^{tm4(ACTB-tdTomato,-EGFP)Luo}$/J; Stock: 007676). *Nestin-CreER*^{T2}, *Gli1-CreER*^{T2}, or *Ascl1-CreER*^{T2} were crossed to fluorescent reporter mice for clonal analysis. *Nestin-CreER*$^{T2+/-}$*::Z/EG*$^{f/+}$ animals were generated by breeding *nestin-CreER*$^{T2+/-}$ and *Z/EG*$^{f/+}$ mice or *nestin-CreER*$^{T2+/-}$*::Z/EG*$^{f/+}$ with wild-type C57BL/6 mice. *Gli1-CreER*$^{T2+/-::}$*Z/EG*$^{f/+}$ or *Gli1-CreER*$^{T2+/-}$*::mT/mG*$^{f/+}$ animals were generated by crossing *Gli1-CreER*$^{T2+/-}$ mice and *Z/EG*$^{f/+}$ or *mTmG*$^{f/f}$, respectively, or by breeding *Gli1-CreER*$^{T2+/-}$*::Z/EG*$^{f/+}$ or *Gli1-CreER*$^{T2+/-}$*::mT/mG*$^{f/f}$ with wild-type C57BL/6 mice. *Ascl1-CreER*$^{T2+/-}$*::YFP*$^{f/+}$or *Ascl1-CreER*$^{T2+/-}$*::mTmG*$^{f/+}$ mice were generated by crossing *Ascl1-CreER*$^{T2+/-}$ with *YFP*$^{f/f}$ or *mTmG*$^{f/f}$, respectively (Figures 1B-C). At least 3 animals were checked for all reporter/driver combinations to assure there was no recombination in the adult SGZ in the absence of tamoxifen. Stock tamoxifen (62 mg/ml; Sigma; T5648) was made with a 5:1 ratio of corn oil/ethanol and heated to 37°C with periodic mixing. For lineage tracing under basal conditions, eight to twelve week-old mice were i.p. injected with a single dose of tamoxifen or vehicle at various concentrations (Table 1). No signs of distress were observed in injected animals. We did not detect any obvious difference in densities of MCM2$^+$ proliferating cells or DCX$^+$ immature neurons in the adult dentate gyrus of *Gli1-CreER*^{T2} (95 ± 8% for MCM2$^+$ cells and 117 ± 2% for DCX$^+$ cells; n = 3) or *Ascl1-CreER*^{T2} knock-in mice (80 ± 6% for MCM2$^+$ cells and 90 ± 4% for DCX$^+$ cells; n = 3) compared to *Nestin-CreER*^{T2} transgenic mice, suggesting a lack of gross haploinsufficiency effect on adult hippocampal neurogenesis.

Primer sets from original publications were used to identify genetically modified mice[43-48]. Genomic tail DNA was isolated in 25 mM NaOH, 0.2 mM EDTA and run for 35 PCR cycles. Z/EG mice were phenotyped in X-gal reactions [50 mM $K_3Fe(CN)_6$, 50 mM $K_4Fe(CN)_63H_2O$, 1 M $MgCl_2$, 10 mg/ml X-Gal in PBS] for 4 hours to overnight.

For AraC treatment-induced injury, *Gli1-CreER*$^{T2+/-}$*::mT/mG*$^{f/+}$, *Ascl1-CreER*$^{T2+/-}$*::mT/mG*, *Nestin-CreER*$^{T2+/-}$*::ZE/G*$^{+/-}$ mice of at least 6 weeks of age were injected with a clonal dose of tamoxifen (Table 1) and housed for 3 to 7 days following tamoxifen injection to avoid killing RGLs in a proliferative state (Figures 17A and 20A). AraC stock solution (1X, 2% weight per volume, 82 mM) was made by adding 5 ml of 0.9% 0.22 µm filtered sterile saline to the 100 mg bottle of AraC (Sigma C1768). Pumps (Alzet Model 1007D Duret brain infusion kit 3) were assembled using sterile procedures. A supplied syringe tip was used to fill the pump with AraC and one spacer was placed on the needle at a 0.5 mm thickness. Pumps were then incubated overnight at 37°C in 0.9% saline. Animals were anesthetized using ketamine; xylazine; acepromazine (100 mg/kg; 15 mg/kg; 1.25 mg/kg Henry Schein; Lloyd; Behringer Inglheim vetmedica Inc.) and buprenex (0.02 mg/kg, Reckitt Benckiser Healthcare UK Ltd.). Miniosmotic pumps were inserted into the mouse right hemisphere at the coordinates of 0.75 mm medial lateral and -0.5 mm posterior using a stereotaxic injection machine and secured to the skull with superglue (Loctite 454). The incision was sutured. The osmotic pump was allowed to infuse for 4 days with mice under normal housing conditions. Three days after pump installation, two shots of EdU (41.1 mg/kg body weight) 2 hours apart were delivered to assess the removal of cell proliferation. EdU labelling was performed with a Click-iT EdU Alexa Fluor imaging kit (Invitrogen). To stop drug flow, mice were anaesthetized and the osmotic pump was removed. Mice were once again housed for another 7 days before analyses. Injury sham control animals were induced with the same level of tamoxifen and given the same anesthesia but were otherwise uninjured when performing clonal analysis. Injury was assessed both by EdU elimination in the SGZ and by GFAP staining for reactive gliosis (Figures 17B-C). Regions distal to the injection site containing reactive gliosis were processed for clonal analysis in *Nestin-CreER*^{T2}, *Gli1-CreER*^{T2} lines. The *Ascl1-CreER*^{T2} line permitted clonal analysis beyond areas of reactive gliosis.

Immunostaining, Confocal Imaging, and Processing

Mice were anesthetized and transcardially infused with saline and then 4% paraformaldehyde. Brain sections were sectioned coronally (45 µm thickness) and maintained in serial order throughout the entire dentate gyrus using custom, in-house staining chambers. Immunohistology was performed using antibodies as previously described[23, 49]. Cre staining was performed using TSA amplification (Cat# NEL704A001KT, Perkin Elmer). Sections were washed in PBS with 0.3% Triton X-100. Endogenous peroxidase activity was quenched with 0.3% Hydrogen Peroxide in PBS for 10 minutes. Sections were blocked for 1 hour in TNB buffer (0.1 M TRIS-HCL pH7.5, 0.15 M NaCl, 0.5% blocking reagent) then incubated overnight in 1:12000 rabbit anti-Cre antibody [47]. Sections were washed and incubated with Biotin-SP-Donkey anti-rabbit secondary antibody (1:200; Cat #711-065-152; Jackson Immuno) in TNB buffer for 2 hours. Sections were washed and then incubated in SA-HRP (1:100) in TNB buffer for 30 minutes. Sections were washed and then incubated 6 minutes in fluorophore tyramide (1:50) in 1X amplification diluent. After a final wash, sections were counterstained, mounted and imaged. The following antibodies were also used: nestin (1:500, chicken; Cat#NES; Aves), GFAP (1:2000, rabbit; Cat#Z0334, DAKO), Ascl1 (1:250, mouse; Cat#556604, BD Pharmingen), DCX (1:500, goat; Cat#SC-9066; Santa Cruz).) Antigen retrieval for MCM2 and Nestin antibodies utilized DAKO citrate buffer (Dako S1699) at 95 ^{o}C for 20 minutes and then left cooled at room temperature.

GFP^{+} cells were identified with an Axiovert 200M microscope (Zeiss) and then acquired as z-stacks on Zeiss 710 single-photon confocal microscope using 40X or 63X objectives. To facilitate 3D reconstructions of GFP^{+} cells spanning multiple sections, optical stacks were taken of the entire clone then serially aligned with Reconstruct 1.1.0 (John C. Fiala, Human Brain Project, the National Institutes of Health) as previously described [23]. To achieve alignment between images of adjacent physical sections, the last of the 2D optical images of one section was translated and rotated in the X-Y plane to match those of the subsequent section. Recorded keystrokes were propagated to all preceding optical sections within the Z-stack. This process was repeated across all Z-stacked confocal images to reconstruct entire clone across multiple sections. Full resolution aligned images were exported into Imaris 7.1.1 (Bitplane) with voxel sizes adjusted according to dimensions specified in the LSM file for visualization of reconstructed clone in 3D.

Clonal Analysis

Clonal analysis was performed as previously described [23]. Cell types were defined by morphological and immunohistological criteria as previously described [23]. Precursors were defined as both RGLs and IPCs in assessing initial induction enrichment (Figure 2A). Clonal distances measurements were made using Imaris (Bitplane), and an in-house MATLAB script to determine distances in 3D. A clone was defined as consisting of cells located within a radius of 150 μm from the clone center. Consistent with criteria used previously [23] approximately 6-18 clones per dentate allowed for clonal analysis based on computer simulation. Clones were induced randomly throughout the dentate, showing no preferential distribution among anterior-posterior, medial-lateral and suprapyramidal-infrapyramidal locations. To confirm consistent level of induction, the number of clones per dentate was assessed at varying time points following induction, which was shown to be comparable over time (Figure 2C). At short time points (0.5 - 1 dpi) clones were single cells or dividing clusters of cells indicative of initial labeling of one cell. Active, dividing clones were defined as clones that underwent division as assessed by having two clear nuclei by DAPI using confocal microscopy (Figures 3A-B). When assessing cell division, two nuclei were either completely encompassed (in the case of the membrane bound reporter mT/mG) or filled (in the case of Rosa-YFP or Z/EG reporter) by the GFP signal in 3D. MCM2 staining was additionally used as a mitotic marker to confirm proper scoring during lineage-tracing (Figures 9A-C). Short time points ($Ascl1^{\#}$ at 1 dpi; $Gli1^{\#}$ at 3 dpi) were chosen to confirm consistency among different reporter mouse lines (Z/EG, YFP, mT/mG; Figures S2D-G). Clones were categorized according the clone composition among RGL-containing clones[23, 50]. For all time points, RGL maintenance was assessed as percent of clones that contained at least one RGL (Figure 10C).

Lineage trees were generated from clones containing RGLs and progeny (Figures 5A-B, 11A-B, 19A-B). Progeny were identified using morphological and immunohistological criteria as previously described [23]. Each fate choice (R-R, R-N, R-A) was considered as a separate division at shorter time points (1, 3, 7 dpi). Repeated RGL-IPC divisions were scored if the clone contained an IPC cluster that migrated away and the RGL must be in the midst of RGL-IPC division. Order of division was assessed by inverse spatial proximity of progeny to RGL such that progeny at a greater distance were considered an earlier division. For longer chase at 30 dpi, lineage trees additionally accounted for the appearance of immature neurons, mature neurons and transition astrocytes. The presence of an IPC/neuroblast (small compact soma with tangential process), immature neuron (DCX^+ radial process), and mature neuron (large soma, radial morphology with elaborate dendrites/spines) were scored as a separate division due to prolonged developmental kinetics during adult hippocampal neurogenesis[51, 52]. We did not reconstitute lineage tree at later time points because of ambiguity to identify RGL division modes. *Gli1-CreER*^{T2} and *Ascl1-CreER*^{T2} lines allowed for birth-dating the first division before AraC treatment and assessment of RGL activation, cell cycle re-entry and lineage trees after injury (Figures 18C and 19A-B). When random cell cycle entry did not make birth-dating possible (*Nestin-CreER*^{T2}), any division before AraC treatment was also included in the analysis (Figure 20). Fraction of division quantification was derived from computational analysis and also included division modes prior to AraC treatment (Figures 18D and 19C). RGL killing in the *Ascl1-CreER*^{T2} line was assessed by the number of RGL-containing clones in control versus AraC conditions 0 and 7 days after completion of AraC treatment (Figure 21A).

Theory

To consolidate the discussion in the main text, in the following we further explain the fitting and modelling approaches used.

Distribution of activation times

The activation time of a RGL is the time until it first enters cell cycle (T_{entry}). To deduce the distribution of activation times from the clonal data, we calculated at each time point the fraction of RGLs that had not yet divided.

As the labelling protocols targeted a small proportion of IPCs in addition to RGLs, there was a degree of error involved in our assignment: we could not decide unambiguously whether a clone consisting entirely of IPCs and differentiated cell types was originally derived from an RGL or an IPC. In the case of Gli1-CreER^{T2} and Ascl1-CreER^{T2} clonal data, the number of such clones was so small that their exclusion would not significantly affect on our results. For Nestin$^{\#}$-RGL, 10/34 clones consist only of 1-2 IPCs at 2 dpi; we assumed that these were IPC-derived and excluded them from the analysis. By 7 dpi, due to the short cell cycle time of IPCs[53, 54], we would expect IPC-derived clones to have grown in size; we therefore took clones containing 6 or more IPCs to be IPC-derived (2/40), and clones consisting only of 2 IPCs to be RGL-derived (4/40). At later time points, we assumed that all clones were RGL-derived. As a second caveat, a clone consisting of a single RGL was scored as an undivided RGL, but may have given rise to progeny that were subsequently lost through cell death. However, effects of any erroneous assignments were likely negligible compared to experimental noise over this timescale.

For a population of cells that divide stochastically at a constant rate λ, the fraction of undivided cells at time t, denoted $R^0(t)$, decays exponentially over time according to $R^0(t) = e^{-\lambda t}$. For all three labelling protocols, exponential decay curves provided excellent fits to the experimental data (Figures 14A-C). By performing a weighted least-squares fit, we deduced that Nestin$^{\#}$-RGL enter cell cycle at a rate λ = 0.044 ± 0.005, equivalent to a mean cell cycle time of $1/\lambda$ = 23 ± 3 days. Similar fits to the early-time Gli1-CreER^{T2} and Ascl1-CreER^{T2} data suggested mean activation times of 0.78 ± 0.02 days and 0.35 ± 0.04 days, respectively (Figure 13B).

Distribution of cell cycle re-entry times

Similarly to RGL activation times, we can estimate cell cycle re-entry times from the fraction of cells that have divided exactly once. For a population of cells with activation rate λ and cell cycle re-entry rate μ, we can show that the fraction of cells divided once at time t, denoted $R^1(t)$, takes the form

$$R^1(t) = \frac{\lambda}{\mu-\lambda}\left(e^{-\lambda t} - e^{-\mu t}\right).$$

For Ascl1$^{\#}$-RGLs and Gli1$^{\#}$-RGLs, divisions were scored based on the ability to clearly identify newly generated cell types. At early time points (1, 3, 7 dpi), RGL-containing clones contained additional RGLs, IPCs and astroglia, whereas at 30 dpi immature neurons (INs), mature neurons (MNs) and transition astrocytes (TAs) additionally appeared. Generation of each cell type was scored as a unique division due to their kinetics along the neuronal lineage ranging from IPCs, INs to MNs [55]. Likewise, the same analysis was applied to non neuronal lineages due to discrete fate specification of new RGLs and the astroglial lineage [23]. Conservatively, each cell type along the neuronal and astroglia lineage was scored as 1 division irrespective of cell number within each category. In cases where multiple cell types were present, the order of cell generation was defined by (i) an anti-correlate of distance from the RGL and (ii) the anti-correlate of maturation through the lineage.

Given our estimates of the activation times, weighted least-squares fits suggested cell cycle re-entry times of $1/\mu$ = 33 ± 7 days for Nestin$^{\#}$-RGLs, 53 ± 12 days for Gli1$^{\#}$-RGLs and 5.3 ± 0.8 days for Ascl1$^{\#}$-RGLs (Figures 13C and 14D-F).

Fate choice probabilities of Nestin$^{\#}$-RGL

Since the estimated re-entry time into cell cycle of Nestin$^{\#}$-RGL is close to their activation time, we assumed in the following that Nestin$^{\#}$-RGL may be modelled as stochastically entering into cell cycle (with the timing between consecutive cell divisions statistically uncorrelated – Markovian) at a constant rate up to 60 dpi.

We next turned to the question of how their fate choices may be inferred from the lineage data. At every division, an RGL produces two daughter cells, choosing two out of the different cell types it could in principle generate. Previous work has shown that RGLs can directly give rise to RGLs, IPCs, transition astroglia (TA), and astroglia (A) [23]. We may ask whether these fate decisions are made stochastically, or whether there is evidence for a predetermined program.

For an ensemble of clones with varying cellular composition, we can define the probability $P_{\{comp\}}(t)$ that any given clone will have a particular composition $\{comp\}$ at a time t after induction. This probability evolves over time according to the transitions between different cell types. For a population of equipotent cells dividing stochastically according to the same constant division rate and fixed probabilities of fate choices, its evolution may be captured mathematically through a master equation. As IPCs divide rapidly and many die[26, 56], it is not currently feasible to infer the dynamics within the neuronal lineage from the clonal data. However, we were only concerned with the fate choices of RGLs, which may be inferred from the RGL and TA/A cell counts alone. We needed only to distinguish among RGL self-renewal (R), differentiation down the neuronal lineage (I), and down the astroglial lineage (A). The corresponding fate choice probabilities for RGL divisions are denoted by r_{RR} for divisions that give rise to two RGL, r_{RI} for divisions that gives rise to one RGL and one cell of the neuronal lineage, etc. The master equation for the probability $P_{m,n}(t)$ that a clone contains m RGLs and n TA/A at time t can be written as

$$\begin{aligned}
\frac{dP_{m,n}(t)}{dt} &= \lambda\big\{r_{RR}\big((m-1)P_{m-1,n}(t)-mP_{m,n}(t)\big)+r_{RA}\big(mP_{m,n-1}(t)-mP_{m,n}(t)\big) \\
&\quad +r_{II}\big((m+1)P_{m+1,n}(t)-mP_{m,n}(t)\big)+r_{AA}\big((m+1)P_{m+1,n-2}(t)-mP_{m,n}(t)\big)+r_{IA}\big((m+1)P_{m+1,n}(t)-mP_{m,n}(t)\big)\big\} \\
&= \lambda\big\{r_{RR}(m-1)P_{m-1,n}(t)+r_{RA}mP_{m,n-1}(t)+(m+1)\big(r_{II}P_{m+1,n}(t)+r_{AA}P_{m+1,n-2}(t)+r_{IA}P_{m+1,n}(t)\big) \\
&\quad -mP_{m,n}(t)\big(r_{RR}+r_{RA}+r_{II}+r_{AA}+r_{IA}\big)\big\},
\end{aligned}$$

where λ is the constant rate of cell division.

Numerically integrating the master equation and computing the resulting clone size distributions, we obtained very good agreement with experimental data (Figure 15). This suggests that Nestin$^{\#}$-RGLs do indeed behave as a population of stochastically dividing stem cells, with no evidence for a deterministic program. Least-squares fitting to the RGL and TA/A content of clones results in a division rate $\lambda = 0.04$, equivalent to a cell cycle time of $1/\lambda = 25$ days. The corresponding fate choice probabilities are given in Figure 13D. As the clone size distributions are well approximated by the fit, the model prediction for the average RGL and TA/A content of clones is also consistent with the data (Figure 15A).

The clonal data for Nestin$^{\#}$-RGL is thus consistent with a model in which RGLs constitute an equipotent population of cells that divide stochastically according to constant fate choice probabilities, at least over the 60 day time course. While it is, of course, possible that more complicated models might fit the data equally well, we can gain confidence in our conclusion from four independent self-consistency checks of our model:

- First, we note that the cell cycle time obtained by fitting the solution of the master equation to the experimentally observed clone size distributions is consistent with our earlier estimate from the fraction of undivided RGLs.
- Second, the probability of symmetric RGL self-renewal is exactly balanced by the total probability of RGL loss due to differentiation ($r_{RR} = r_{II} + r_{AA} + r_{IA}$). We would therefore predict that the average number of RGLs per clone remains close to 1, which is indeed the case (Figure 15A).
- Third, we expect on theoretical grounds that the fraction of persisting clones, i.e. clones that retain at least one RGL at time t, should follow a power-law decay of the form $1/(1+r_{RR}\lambda t)$ [57]. The data is consistent with this prediction (Figure 15B).
- Fourth, we can compare the fate choice probabilities obtained from the fit with those inferred directly from the clonal data. To this end, we assign to every RGL-derived clone in the 2, 7 and 30 dpi Nestin$^{\#}$-RGL data the first division likely undergone by the initially labeled RGL (n = 33). Our assignments are subject to some ambiguity; in particular, RGL self-renewal followed by differentiation of one or both daughter cells could be erroneously scored as a differentiating division. Comparing two sets of parameters, the fate choice probabilities found in this way indeed suggest a lower value for r_{RR} than predicted by the fit, but overall the results are roughly consistent (Figure 15C).

Over the first 60 days following induction, the clonal data for Nestin$^{\#}$-RGL is thus consistent with a model in which RGLs constitute an equipotent population of cells that divide stochastically according to constant fate choice probabilities. However, it is also obvious from the data that RGL self-renewal is limited within a clone and becomes more pronounced by 120 dpi. Following the initial stochastic expansion of clones, unknown factors limit the number of RGLs within a clone in the long term.

Fate choice probabilities of Gli1$^{\#}$-RGL and Ascl1$^{\#}$-RGL

As the activation (T_{entry}) and re-entry times (T_c) of Ascl1$^{\#}$-RGL and Gli1$^{\#}$-RGL differ markedly, we cannot apply the same master equation approach we employed for the Nestin$^{\#}$-RGL data, which assumes a constant average time between divisions. Instead, we estimated their fate choice probabilities directly from the clonal data in the same way as we did for Nestin$^{\#}$-RGL. We inferred the first division of labeled RGL at 1 dpi for Ascl1$^{\#}$-RGL and at 1-3 dpi for Gli1$^{\#}$-RGL, choosing different time windows due to the slower activation time of Gli1$^{\#}$-RGL (n = 76 for Ascl1$^{\#}$-RGL and 88 for Gli1$^{\#}$-RGL). As discussed in the main text, fate choice probabilities differed significantly between Gli1$^{\#}$-RGL and Ascl1$^{\#}$-RGL, with the latter displaying an obvious bias towards the neuronal lineage (see also Figure 13D). Interestingly, the fate choice probabilities of Gli1$^{\#}$-RGL were roughly consistent with those of Nestin$^{\#}$-RGL. It is therefore conceivable that the two labeling protocols target the same population, with Gli1$^{\#}$-RGL labeling RGLs that are about to enter cell cycle.

To resolve whether the Gli1$^{\#}$-RGL clonal data is consistent with the Nestin$^{\#}$-RGL dynamics, we simulated the time evolution of 10,000 RGLs that enter cycle according to the Gli1$^{\#}$-RGL activation time, but subsequently evolve according to the Nestin$^{\#}$-RGL division rate and fate choice probabilities. At every time point, a number of clones equivalent to that observed experimentally is selected at random, and the resulting clone size distributions are computed. Repeating this process 5,000 times, we calculated the average expected clone size distributions as well as 95% plausible intervals. We found that the Gli1$^{\#}$-RGL clonal data is indeed consistent with the Nestin$^{\#}$-RGL dynamics (see Figures 14G-I). The average RGL and TA/A content of clones are also well predicted by the model over 30 day period (Figure 15D). Beyond 30 days, we observe less good agreement with the stochastic model. Taking into account the offset in activation times, this mirrors our observations in the Nestin$^{\#}$-RGL data up to 120 days.

In contrast to the Nestin$^{\#}$-RGL and Gli1$^{\#}$-RGL data, no combination of division rate and fate choice probabilities results in a satisfactory fit of the same model to the Ascl1$^{\#}$-RGL data, suggesting that Ascl1$^{\#}$-RGLs do not behave as a population of stem cells cycling at a constant rate and with fixed fate choice probabilities. For example, assuming that Ascl1$^{\#}$-RGLs keep dividing at the estimated cell cycle re-entry rate and with the fate choice probabilities determined above, the model predicts that RGL would be lost faster and more TA/A would have been generated by 30 dpi (Figure 15E).

In summary, the data obtained from the three labeling protocols thus suggests that activating RGLs conform to one of two populations in the two-month period we examined: a fast-cycling cohort in which RGL are strongly biased towards neuronal differentiation, and a slower-cycling group with more balanced fate choice probabilities.

Statistics

The student's t-test was used to generate p-values to compare data as indicated. For computational analysis, all clones observed at each time point were treated as statistically equivalent. Standard errors in mean frequencies were estimated as $\sqrt{p(1-p)/N}$, where p is the frequency of a given characteristic at a time point and N the number of clones considered. Fits were performed by weighted least squares using custom-written scripts in MATLAB (MathWorks, Inc.).

3 Results

3.1 Labeling of Radial Glia-like Precursors in Different Activation States

Previous studies have used various transgenic mouse lines to fate-map RGLs in the adult dentate gyrus at the population level (Figure 1A) [22], including *Nestin-CreER*^{T2} [24, 37], *Gli1-CreER*^{T2} [43], and *Ascl1-CreER*^{T2} [44]. RGLs labeled in these lines exhibit grossly similar morphological and immunohistological characteristics. To investigate their functional properties, we developed single-cell lineage-tracing approaches using *Gli1-CreER*^{T2} and *Ascl1-CreER*^{T2} following our previous strategy for *Nestin-CreER*^{T2}-based clonal analysis [23]. For each CreER^{T2} driver, we tested different tamoxifen doses and reporter lines, including Z/EG [46], mT/mG [48], and Rosa-YFP[58], and obtained combinations that exhibited high specificity, inducibility and reproducibility (Figures 1B-C and Table 1). At one day post-tamoxifen induction (dpi), over 90% of labeled precursor cells within the adult dentate gyrus of each line were Nestin^{+}GFAP^{+} RGLs with soma in the SGZ and basal branches extending through the granule cell layer into the molecular layer (n = 3; Figures 2A-B). Approximately 6-18 precursors were labeled per dentate gyrus at 1 dpi and the number of cell clusters remained generally constant over the period of analysis, whereas the clonal size increased over time (Figures 2C-D). Previous computational simulations have suggested over 95% probability of clonality with this initial labeling density in the adult dentate gyrus [23].

Upon establishing high fidelity clonal lineage-tracing of RGLs with two independent approaches, we first examined the activation of labeled RGLs based on short-term lineage analysis. At 7 dpi nearly all Gli1$^{\#}$-RGL and Ascl1$^{\#}$-RGL clones already contained adjacent progeny, indicative of RGL activation (Figures 3A-B). This result is in sharp contrast to previous findings of Nestin$^{\#}$-RGLs, few of which divide within 7 dpi [50]. Further time-course analysis showed that most Gli1$^{\#}$-RGL clones contained a single RGL without any progeny at 0.5 dpi, the earliest time point to detect sufficient GFP expression, and nearly all produced progeny by 3 dpi

(Figure 3C). In contrast, Ascl1$^{\#}$-RGL clones already contained progeny at 1 dpi (Figure 3D), consistent with a recent population-level fate-mapping study[59]. To estimate the cell cycle status at the time of labeling, we performed immunohistological analysis of RGLs with Cre antibodies. Consistent with the short-term lineage result, 17.6 ± 2.4% and 70.3 ± 1.2% of Cre^{+} RGLs were MCM2^{+} in the dentate gyrus of adult *Gli1-CreER*^{T2} and *Ascl1-CreER*^{T2} mice, respectively (Figures 4A and 4C). Interestingly, Ascl1 immunostaining showed that 14 ± 2% and 75 ± 2% of Cre^{+} RGLs were Ascl1^{+} in the dentate gyrus of adult *Gli1-CreER*^{T2} and *Ascl1-CreER*^{T2} mice, respectively (Figures 4B-C), suggesting minimal over-lapping of these two populations. Together, these results show that, in contrast to Nestin$^{\#}$-RGLs, which were labeled in a quiescent state, Gli1$^{\#}$-RGLs were labeled in a pre-activation state, whereas Ascl1$^{\#}$-RGLs were labeled in an active state in the adult mouse dentate gyrus. Therefore, our genetic labeling strategies capture different cell cycle states of adult neural precursors in vivo.

Figure 1 Labeling of RGLs in the adult rodent dentate gyrus

(A) Schematic illustration of neural precursor lineage relationships within the adult hippocampus. Colored bars indicate approaches used in this study to lineage trace Nestin$^{\#}$-RGLs, Gli1$^{\#}$-RGLs, and Ascl1$^{\#}$-RGLs at the clonal level. A: astroglial lineage; TA: transition astrocyte; Astro: Astrocyte; N: neuronal lineage; IPC: intermediate progenitor cell; IN: immature neuron; MN: mature neuron

(B-C) Schematic illustrations of genetic approaches used to lineage-trace individual RGLs in the adult mouse hippocampus.

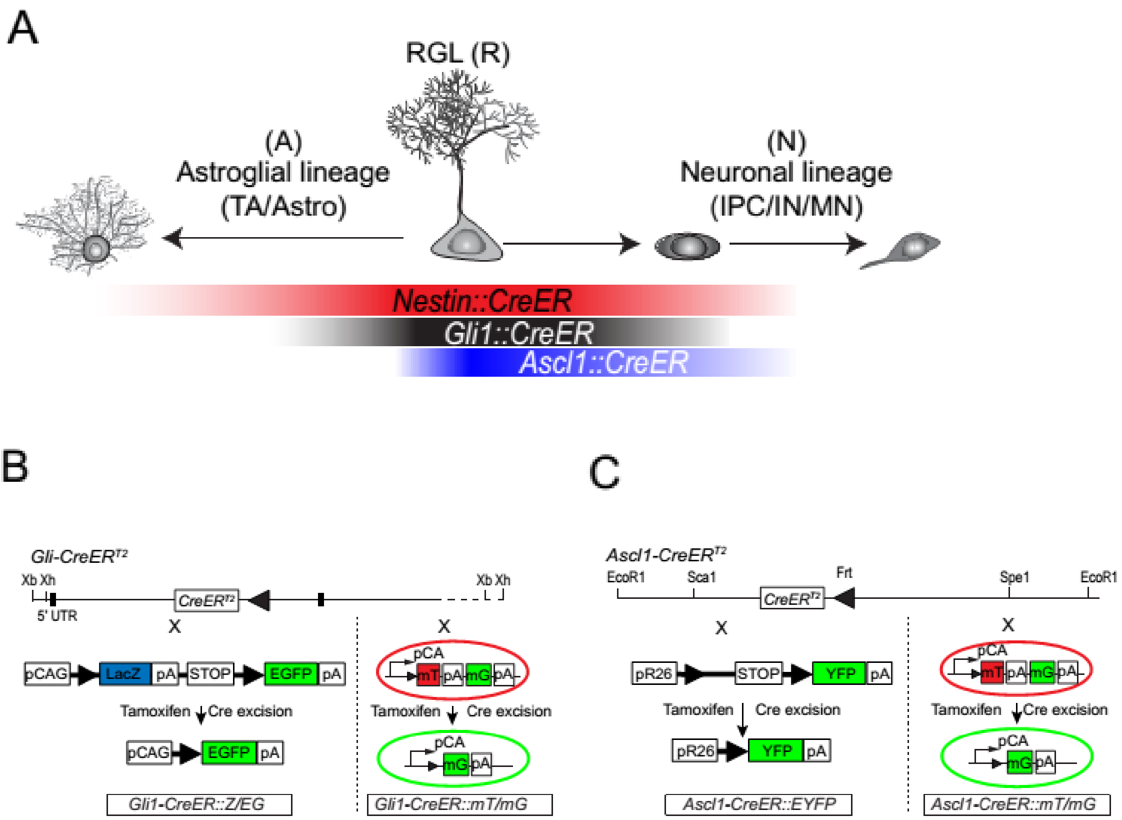
A
RGL (R)
(A)
Astroglial lineage
(TA/Astro)
(N)
Neuronal lineage
(IPC/IN/MN)
Nestin::CreER
Gli1::CreER
Ascl1::CreER
B
Gli-CreER^{T2}
Xb Xh
5' UTR
CreER^{T2}
Xb Xh
X
pCAG
LacZ
pA
STOP
EGFP
pA
Tamoxifen
Cre excision
pCAG
EGFP
pA
Gli1-CreER::Z/EG
X
pCA
mT
pA
mG
pA
Tamoxifen
Cre excision
pCA
mG
pA
Gli1-CreER::mT/mG
C
Ascl1-CreER^{T2}
EcoR1
Sca1
CreER^{T2}
Frt
Spe1
EcoR1
X
pR26
STOP
YFP
pA
Tamoxifen
Cre excision
pR26
YFP
pA
Ascl1-CreER::EYFP
X
pCA
mT
pA
mG
pA
Tamoxifen
Cre excision
pCA
mG
pA
Ascl1-CreER::mT/mG

Table 1 Tamoxifen doses used to achieve clonal recombination among various promoter, reporter and environmental contexts over the analyzed time course

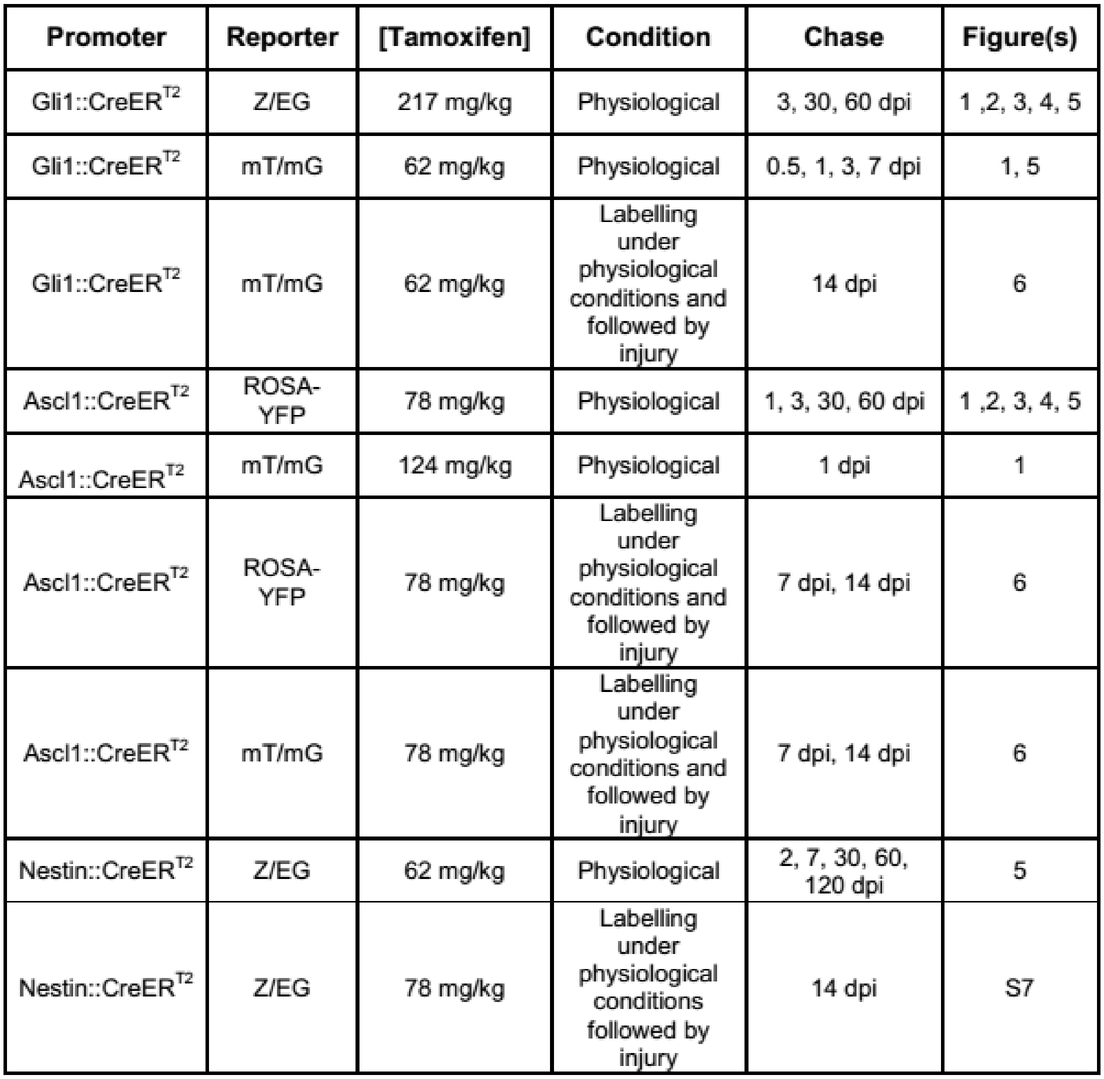

Promoter	Reporter	[Tamoxifen]	Condition	Chase	Figure(s)
Gli1::CreER^{T2}	Z/EG	217 mg/kg	Physiological	3, 30, 60 dpi	1 ,2, 3, 4, 5
Gli1::CreER^{T2}	mT/mG	62 mg/kg	Physiological	0.5, 1, 3, 7 dpi	1, 5
Gli1::CreER^{T2}	mT/mG	62 mg/kg	Labelling under physiological conditions and followed by injury	14 dpi	6
Ascl1::CreER^{T2}	ROSA-YFP	78 mg/kg	Physiological	1, 3, 30, 60 dpi	1 ,2, 3, 4, 5
Ascl1::CreER^{T2}	mT/mG	124 mg/kg	Physiological	1 dpi	1
Ascl1::CreER^{T2}	ROSA-YFP	78 mg/kg	Labelling under physiological conditions and followed by injury	7 dpi, 14 dpi	6
Ascl1::CreER^{T2}	mT/mG	78 mg/kg	Labelling under physiological conditions and followed by injury	7 dpi, 14 dpi	6
Nestin::CreER^{T2}	Z/EG	62 mg/kg	Physiological	2, 7, 30, 60, 120 dpi	5
Nestin::CreER^{T2}	Z/EG	78 mg/kg	Labelling under physiological conditions followed by injury	14 dpi	S7

Figure 2 Clonal lineage-tracing of RGLs in the adult mouse dentate gyrus

(A) Quantification of the percentage of RGLs among GFP$^+$ precursors in the dentate gyrus at 1 dpi. Values represent mean ± SEM (Gli1$^\#$-RGL: n = 4 dentate gyri; Ascl1$^\#$-RGL: n = 8 dentate gyri).

(B) Sample confocal images of Gli1$^\#$-RGL and Ascl1$^\#$-RGL clones at 1 day post-injection (dpi). Immunohistological analysis of GFP$^+$ RGLs showed 100 ± 0% presence of neural precursor markers Nestin and GFAP in both Gli1$^\#$-RGLs (n = 3 animals) and Ascl1$^\#$-RGLs (n = 3 animals). Scale bars, 5 μm.

(C-D) Quantification of the number of clones labeled (C) and number of cells within each clone (D) at different time points post tamoxifen injection using Ascl1$^\#$ and Gli1$^\#$ labeling strategies. Values in (C) represent mean ± SEM ($n \geq 6$ dentate gyri for each time point). Numbers in (D) indicate number of cells in each clone at different time points.

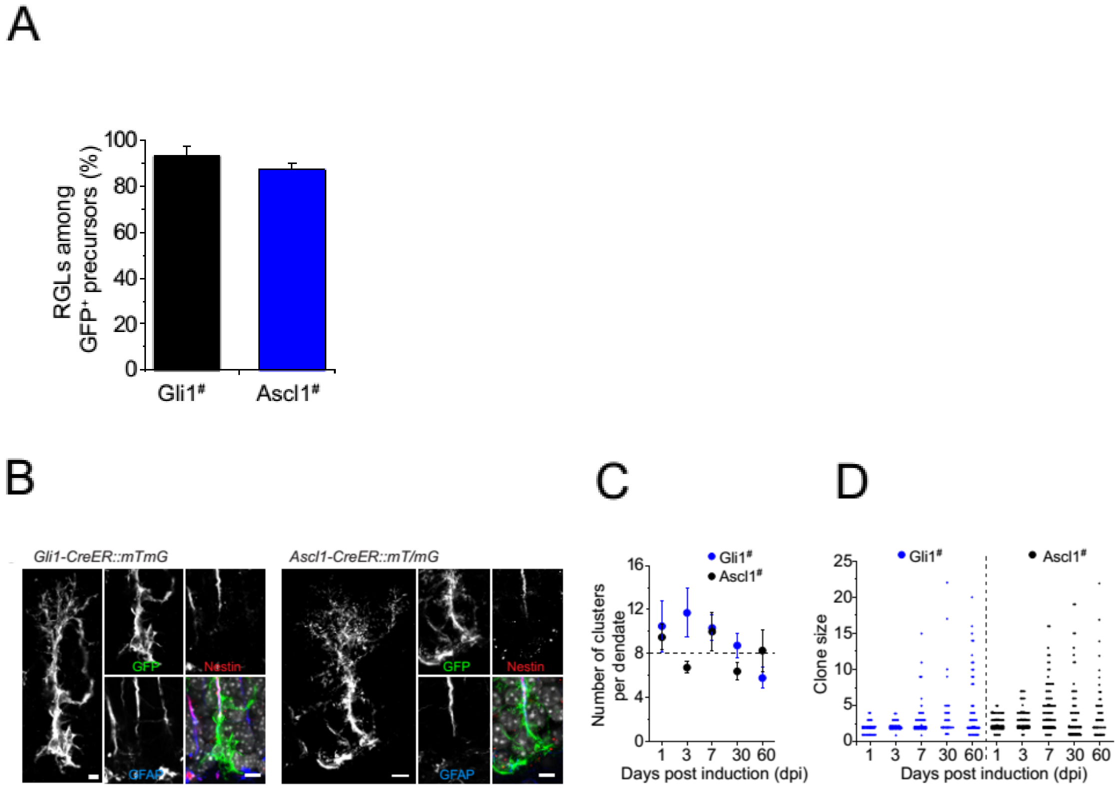
A
RGLs among GFP⁺ precursors (%)
100
80
60
40
20
0
Gli1#
Ascl1#
B
Gli1-CreER::mTmG
GFP
Nestin
GFAP
Ascl1-CreER::mT/mG
GFP
Nestin
GFAP
C
Number of clusters per dendate
16
12
8
4
0
Gli1#
Ascl1#
1
3
7
30
60
Days post induction (dpi)
D
Clone size
25
20
15
10
5
0
Gli1#
Ascl1#
1
3
7
30
60
1
3
7
30
60
Days post induction (dpi)

Figure 3 Labeled RGLs quickly become activated

(A-B) Sample confocal images of GFP-labeled quiescent and activated RGL clones indicated by the presence of more than one DAPI$^+$ nuclei in Gli1$^\#$-RGL (A) and Ascl1$^\#$-RGL (B). Scale bars, 10 μm (5 μm for inserts).

(C-D) Time course of Gli1$^\#$-RGL and Ascl1$^\#$-RGL activation following clonal labeling. RGL activation was scored based on the presence of immediate adjacent progeny. Values represent mean ± SEM (n = 5 - 9 dentate gyri). Red lines represent best fit.

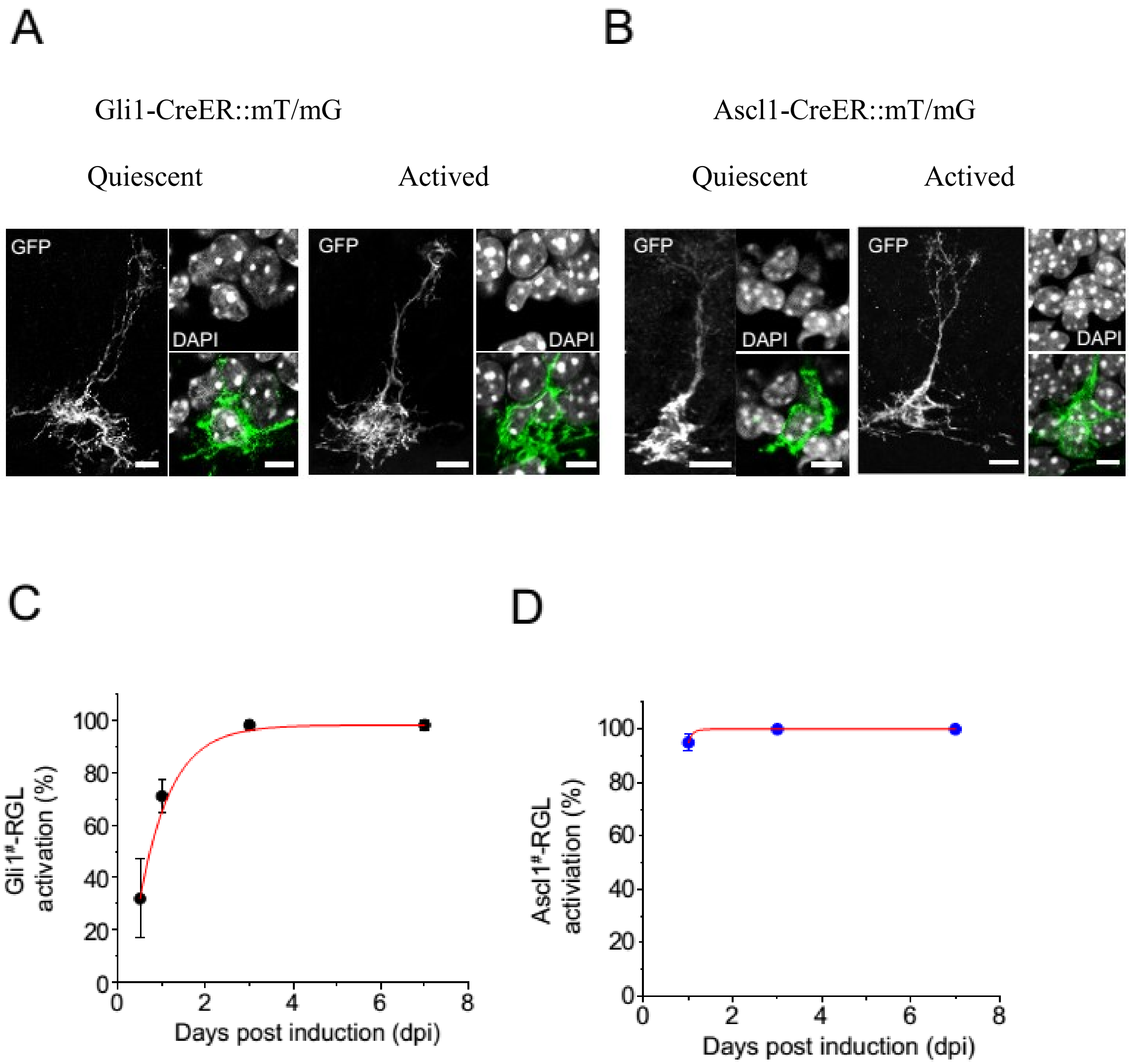
A
Gli1-CreER::mT/mG
Quiescent
Actived
GFP
DAPI
GFP
DAPI
B
Ascl1-CreER::mT/mG
Quiescent
Actived
GFP
DAPI
GFP
DAPI
C
Gli1#-RGL activation (%)
0
20
40
60
80
100
0
2
4
6
8
Days post induction (dpi)
D
Ascl1#-RGL activiation (%)
0
20
40
60
80
100
0
2
4
6
8
Days post induction (dpi)

Figure 4 Characterization of Cre expressing cells in the dentate of CreER mice

(A-B) Sample confocal images of Cre immunohistology in the dentate gyrus of adult CreER mice. Arrows denote Cre$^+$MCM2$^-$ RGLs in *Gli1-CreER*^{T2} mice and Cre$^+$MCM2$^+$ RGLs in *Ascl1-CreER*^{T2} mice (A). Open arrowheads denote Cre$^+$Mash1$^-$ RGLs in *Gli1-CreER*^{T2} mice (B). Scale bars: 100 µm (10 µm for inserts).

(C) Comparison of the percentage of Cre$^+$ RGLs that were MCM2$^+$ or Mash1$^+$ in *Gli1-CreER*^{T2} and *Ascl1-CreER*^{T2} mice. Values represent mean ± SEM (n = 3 dentate gyri; $^*p < 0.001$; Student's t-test).

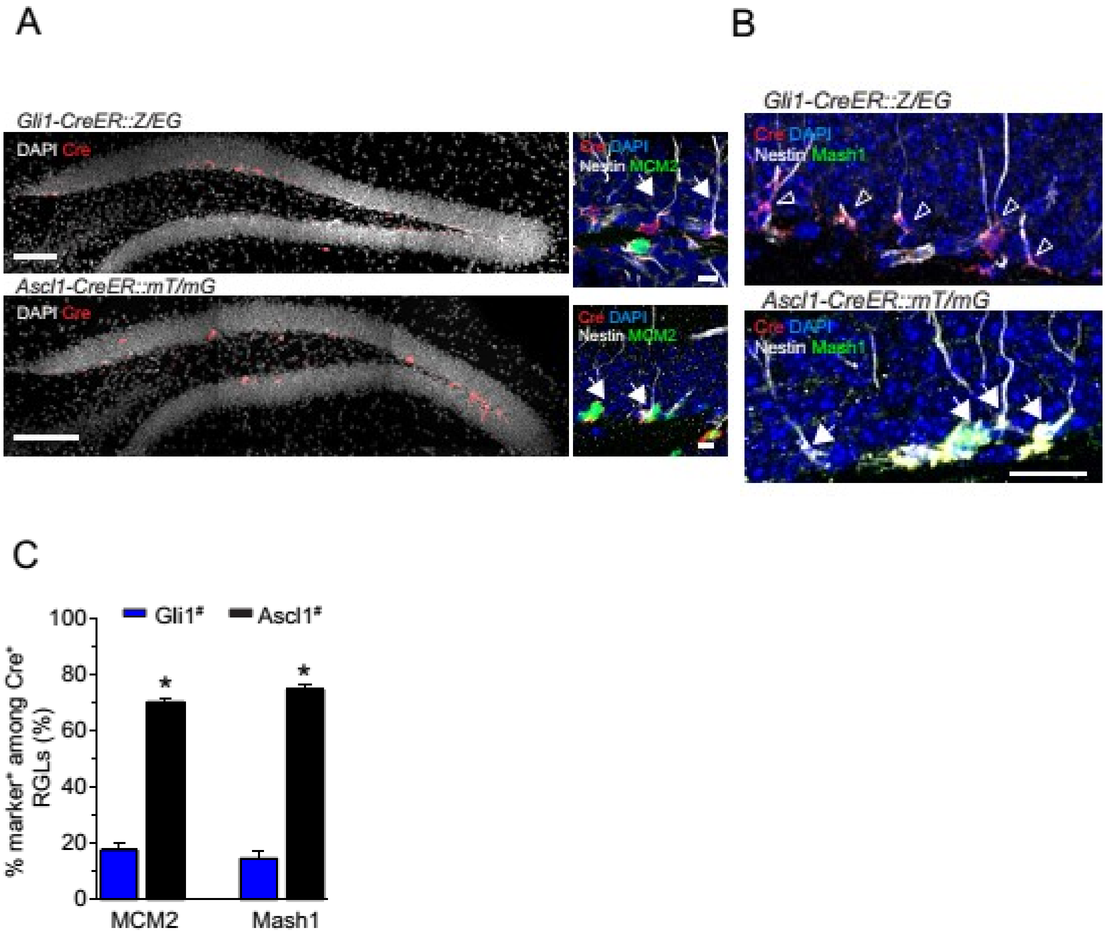
A
Gli1-CreER::Z/EG
DAPI Cre
Cre DAPI
Nestin MCM2
Ascl1-CreER::mT/mG
DAPI Cre
Cre DAPI
Nestin MCM2
B
Gli1-CreER::Z/EG
Cre DAPI
Nestin Mash1
Ascl1-CreER::mT/mG
Cre DAPI
Nestin Mash1
C
Gli1#
Ascl1#
% marker+ among Cre+ RGLs (%)
100
80
60
40
20
0
*
*
MCM2
Mash1

3.2 Fate Choice Bias of Different RGLs

Stem cells are characterized according to their capacity of lineage generation [60]. Nestin$^{\#}$-RGLs in the adult dentate gyrus have previously been shown to undergo three types of self-renewing divisions: symmetric division generating two RGLs, asymmetric neurogenic division producing a GFAP^{-} intermediate progenitor cell (IPC) of the neuronal lineage, and asymmetric astrogenic division resulting in a GFAP^{+} bushy astroglia [23]. One major limitation of the previous *Nestin-CreER*^{T2}-based clonal analyses is a lack of precise birth-dating of quiescent neural stem cells. As a result, their self-renewal modes were largely inferred from retrospective analysis. Since Gli1$^{\#}$-RGLs and Ascl1$^{\#}$-RGLs both divide shortly after labeling (Figures 3C-D), our current approach allows high-resolution direct quantification of fate decisions of adult neural precursor cells in vivo. In addition, fate choices over multiple divisions within a clone can be deciphered based on the type of progeny and distance away from the parent RGL (See Methods). We therefore constructed lineage trees for RGL-containing clones from short-term lineage-tracing, classified according to the progeny generated and the number of divisions the RGL underwent (Figure 5A). Similar to Nestin$^{\#}$-RGLs [23], Gli1$^{\#}$-RGLs exhibited 3 modes of self-renewal division (Figure 5B): symmetric (Figure 6A), asymmetric neurogenic (Figure 6B) and asymmetric astrogenic (Figure 6C). Quantification of 116 Gli1$^{\#}$-RGL clones from 18 reconstructed dentate gyri at 1, 3 and 7 dpi showed 29% symmetric, 45% neurogenic and 26% astrogenic divisions (Figure 6E). In contrast, quantification of 163 Ascl1$^{\#}$-RGL clones from 24 dentate gyri at 1, 3 and 7 dpi indicated that the majority of divisions were neurogenic (76%, Figure 6D) with much lower percentages of symmetric (18%) and few astrogenic (6%) divisions (Figure 6E). Importantly, we obtained similar results with two different reporters for both Gli1$^{\#}$-RGLs and Ascl1$^{\#}$-RGLs (Figure 7). Together, these results indicate that Gli1$^{\#}$-RGLs generate multiple neural lineages, whereas Ascl1$^{\#}$-RGLs are largely neurogenic, revealing additional differences between these two RGLs.

Figure 5 Lineage trees from short-term analyses of Gli1$^{\#}$-RGL and Ascl1$^{\#}$-RGL clones

(A) List of observed lineage trees for Gli1$^{\#}$-RGLs and Ascl1$^{\#}$-RGLs at 1, 3 and 7 dpi. The color scheme denotes the categorization type of lineage trees, which are further subdivided by the number of RGL divisions.

(B-C) Quantification of RGL-containing Gli1$^{\#}$-RGL (B) and Ascl1$^{\#}$-RGL (C) clone types at 1, 3 and 7 dpi. Colors represent the same clone type as denoted in (A).

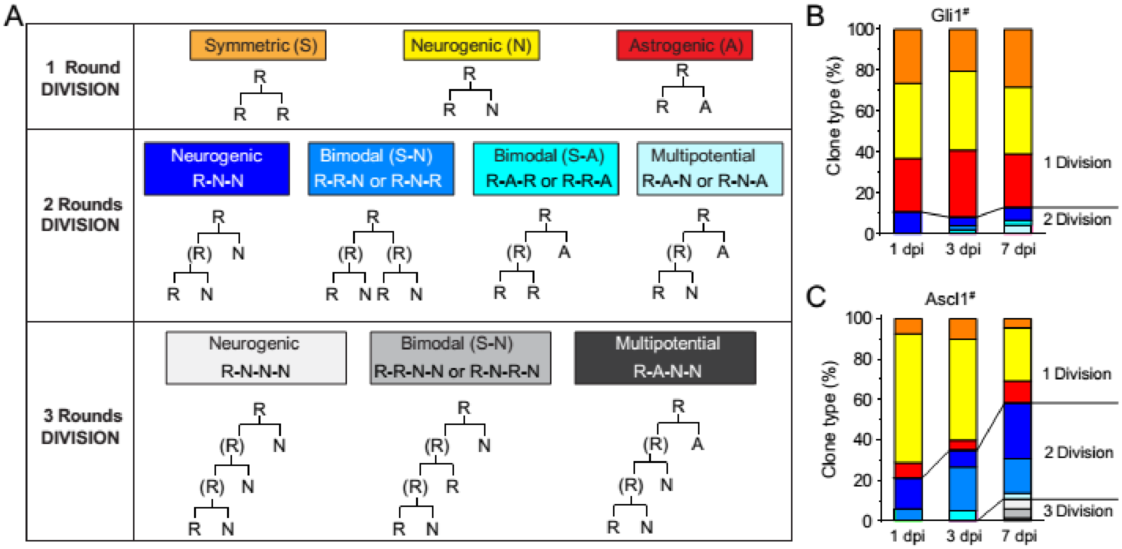
A
1 Round DIVISION
Symmetric (S)
R
R R
Neurogenic (N)
R
R N
Astrogenic (A)
R
R A
2 Rounds DIVISION
Neurogenic R-N-N
Bimodal (S-N) R-R-N or R-N-R
Bimodal (S-A) R-A-R or R-R-A
Multipotential R-A-N or R-N-A
R
(R) N
R N
R
(R) (R)
R N R N
R
(R) A
R R
R
(R) A
R N
3 Rounds DIVISION
Neurogenic R-N-N-N
Bimodal (S-N) R-R-N-N or R-N-R-N
Multipotential R-A-N-N
R
(R) N
(R) N
R N
R
(R) N
(R) R
R N
R
(R) A
(R) N
R N
B
Gli1#
Clone type (%)
100
80
60
40
20
0
1 dpi
3 dpi
7 dpi
1 Division
2 Division
C
Ascl1#
Clone type (%)
100
80
60
40
20
0
1 dpi
3 dpi
7 dpi
1 Division
2 Division
3 Division

Figure 6 Fate specification of Gli1$^{\#}$-RGLs and Ascl1$^{\#}$-RGLs

(A-C) Sample confocal images of representative division modes by Gli1$^{\#}$-RGLs, including symmetric RGL-RGL division (A), asymmetric neurogenic RGL-IPC division (B) and asymmetric astrogenic RGL-Astrocyte division (C). Single confocal section images in inserts highlight newly generated progeny. Orthogonal views are also shown to reveal co-localization of two immunostaining signals. Scale bars, 10 µm (5 µm for inserts).

(D) Sample confocal image of the typical neurogenic RGL-IPC division mode in an Ascl1$^{\#}$-RGL clone. Scale bars, 10 µm (5 µm for inserts).

(E) Quantification of fate choice made by Gli1$^{\#}$-RGLs and Ascl1$^{\#}$-RGLs during 7 days after labeling (combined data from 1, 3, 7 dpi). Values represent mean ± SEM (Gli1$^{\#}$-RGLs, n = 18; Ascl1$^{\#}$-RGLs, n = 24 dentate gyri; $^{*}p < 0.05$, $^{**}p < 0.01$; Student's t-test). R-R: RGL symmetric division; R-N: RGL neuronal asymmetric division; R-A: RGL astrogenic asymmetric division.

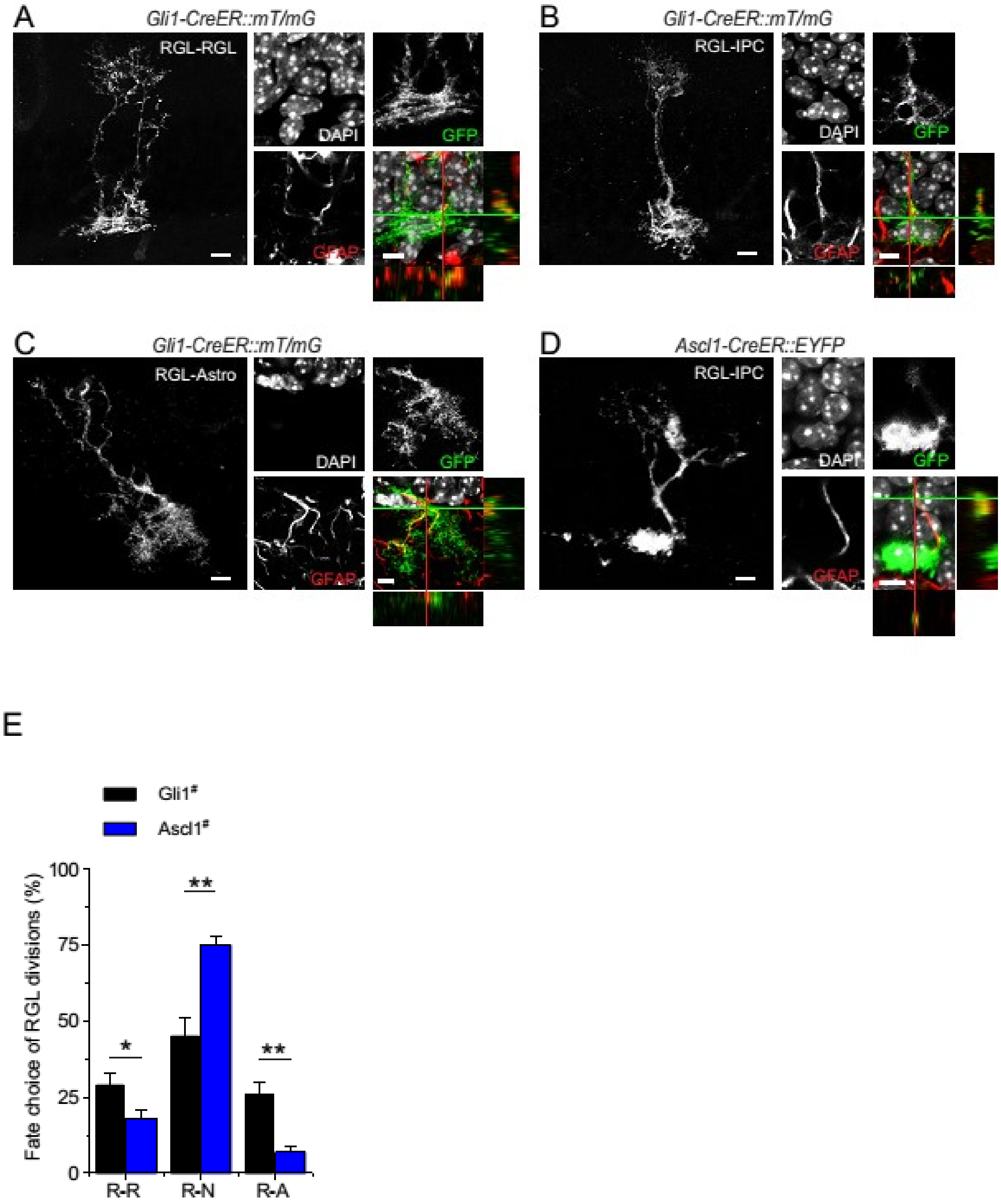
A
Gli1-CreER::mT/mG
RGL-RGL
DAPI
GFP
GFAP
B
Gli1-CreER::mT/mG
RGL-IPC
DAPI
GFP
GFAP
C
Gli1-CreER::mT/mG
RGL-Astro
DAPI
GFP
GFAP
D
Ascl1-CreER::EYFP
RGL-IPC
DAPI
GFP
GFAP
E
Gli1#
Ascl1#
Fate choice of RGL divisions (%)
100
75
50
25
0
*
**
**
R-R
R-N
R-A

Figure 7 Reporter comparisons from short-term analyses of Gli1$^{\#}$-RGL and Ascl1$^{\#}$-RGL clones

(A-D) RGL fate choices assessed by independent lineage-tracing reporter paradigms. Shown are summaries of RGL division types for Gli1$^{\#}$-RGLs in mT/mG or Z/EG reporter mice at 3 dpi (A) and for Ascl1$^{\#}$-RGLs by Rosa-YFP or mT/mG reporter mice at 1 dpi (B). Values represent mean ± SEM.

Also shown are quantification of RGL-containing clone compositions (C-D). The same clones as in (A-B) were quantified.

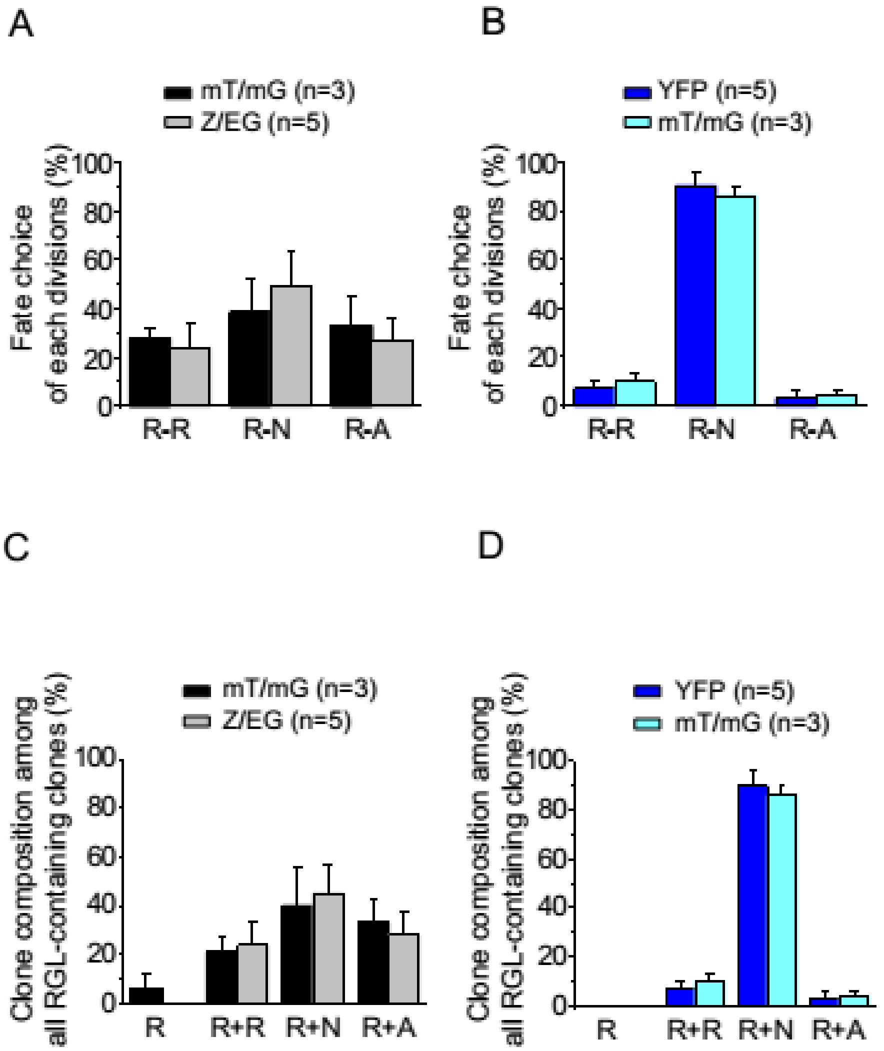
A
mT/mG (n=3)
Z/EG (n=5)
Fate choice of each divisions (%)
0
20
40
60
80
100
R-R
R-N
R-A
B
YFP (n=5)
mT/mG (n=3)
Fate choice of each divisions (%)
0
20
40
60
80
100
R-R
R-N
R-A
C
mT/mG (n=3)
Z/EG (n=5)
Clone composition among all RGL-containing clones (%)
0
20
40
60
80
100
R
R+R
R+N
R+A
D
YFP (n=5)
mT/mG (n=3)
Clone composition among all RGL-containing clones (%)
0
20
40
60
80
100
R
R+R
R+N
R+A

3.3 Divergence in Cell Cycle Exit after Initial RGL Activation

Upon division, RGLs can re-enter cell cycle or return to quiescence[23, 24]. Birth-dating the initial division permits high resolution analysis of cell cycle exit and re-entry. Quantitative short-term lineage analysis revealed marked differences in the number of cell divisions by Gli1$^{\#}$-RGLs and Ascl1$^{\#}$-RGLs within 7 days post-induction (Figures 8A-B and 5B-C). While cell cycle re-entry of Gli1$^{\#}$-RGLs was consistently low from 1 dpi (7 ± 7%) to 7 dpi (13 ± 5%), this fraction for Ascl1$^{\#}$-RGLs increased from 21 ± 4% at 1 dpi to 55 ± 8% at 7 dpi (Figure 8C). Additionally, three rounds of RGL divisions could be observed in Ascl1$^{\#}$-RGL clones during this period, but not in any of Gli1$^{\#}$-RGL clones (Figures 5B-C). To validate results on RGL cell cycle re-entry, we examined MCM2 expression of activated RGL clones at 3 dpi. Indeed, a significantly higher percentage of Ascl1$^{\#}$-RGLs that already had progeny were MCM2^{+} compared to Gli1$^{\#}$-RGLs (Figures 9A-C). Notably, for both Gli1$^{\#}$-RGLs and Ascl1$^{\#}$-RGLs, the percentages of MCM2^{+} RGLs at 3 dpi were consistent with the fraction of RGLs that had divided by 7 dpi based on lineage-tracing (Figures 8C and 9C). These results confirmed that RGLs prospectively identified using MCM2 would divide as assessed by retrospective lineage-analysis. Hence, results from these two independent approaches showed that Gli1$^{\#}$-RGLs largely return to quiescence after activation, whereas Ascl1$^{\#}$-RGLs exhibit an increased probability of cell cycle re-entry, indicative of a more proliferative precursor population.

Figure 8 Divergent cell cycle re-entry property by Gli1$^{\#}$-RGLs and Ascl1$^{\#}$-RGLs

(A-B) Confocal images of Ascl1$^{\#}$-RGL clones with multiple divisions within 7 days. Shown are examples of an Ascl1$^{\#}$-RGL with a neuronal R-N division (1) after a symmetric R-R division (2; A) and an Ascl1$^{\#}$-RGL with multiple neuronal divisions (B). Orthogonal views are also shown. Scale bars, 10 μm (5 μm for inserts).

(C) Quantification of cell cycle re-entry based on lineage analysis at 1, 3 and 7 dpi. Values represent mean ± SEM (n = 5-12 dentate gyri for each time point; *p < 0.01; Student's t-test).

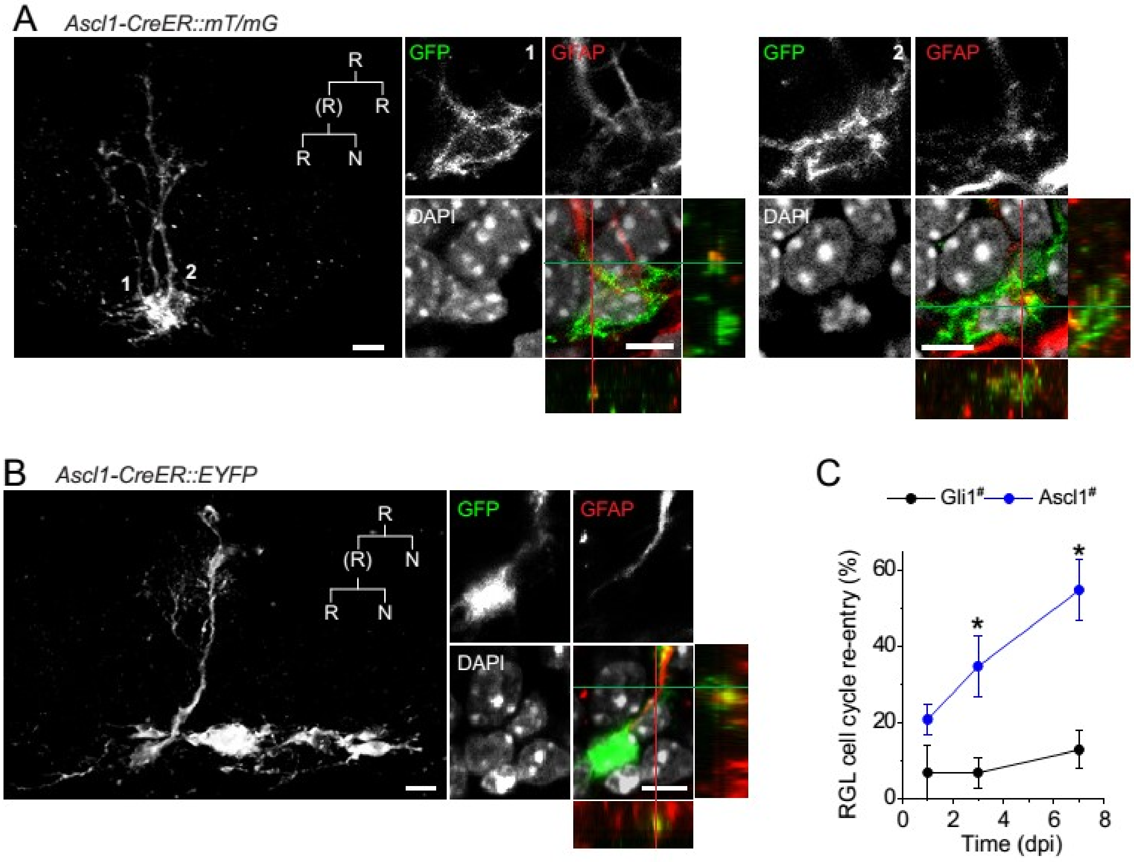
A
Ascl1-CreER::mT/mG
R
(R)
R
R
N
1
2
GFP
1
GFAP
DAPI
GFP
2
GFAP
DAPI
B
Ascl1-CreER::EYFP
R
(R)
N
R
N
GFP
GFAP
DAPI
C
Gli1#
Ascl1#
RGL cell cycle re-entry (%)
60
40
20
0
*
*
0
2
4
6
8
Time (dpi)

Figure 9 Mitotic marker labeling displays re-entry behavior within Ascl1$^{\#}$-RGLs

(A-C) Assessment of cell cycle re-entry of Ascl1$^{\#}$-RGL and Gli1$^{\#}$-RGL clones at 3 dpi with MCM2 immunohistology. Shown are sample confocal images of a quiescent MCM2^{-} Gli1$^{\#}$-RGL (A) and an active MCM2^{+} Ascl1$^{\#}$-RGL (B). Also shown is the quantification of MCM2^{+} RGL clones at 3 dpi (C). Values represent mean ± SEM (n = 3-4 dentate gyri; *$p < 0.01$; Student's t-test).

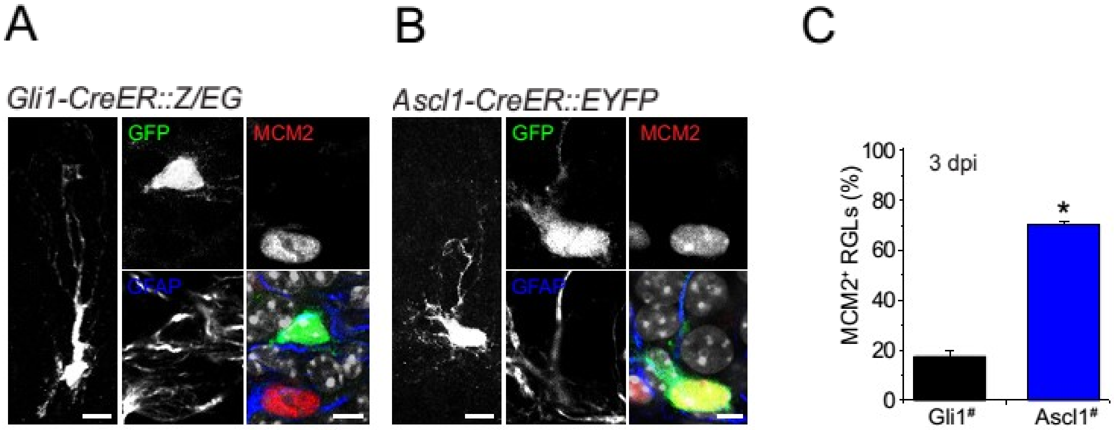
A
Gli1-CreER::Z/EG
GFP
MCM2
GFAP
B
Ascl1-CreER::EYFP
GFP
MCM2
GFAP
C
3 dpi
MCM2+ RGLs (%)
100
80
60
40
20
0
*
Gli1#
Ascl1#

3.4 Maintenance of Distinct Stem Cell Properties by Gli1$^{\#}$-RGLs and Ascl1$^{\#}$-RGLs

In addition to lineage generation, bona fide stem cells are defined by their capacity for self-renewal without differentiating for an extended period of time [2]. While quiescent RGLs are known to persist over long periods at the population and single-cell levels[23, 37], whether RGLs are maintained after division is controversial as it has been suggested that RGL cell cycle entry is coupled to their depletion [24]. To directly examine the maintenance of RGLs after division, we quantified Gli1$^{\#}$-RGL and Ascl1$^{\#}$-RGL clones at 30 and 60 dpi (Figures 10A-B), a sufficient duration to probe the "division-coupled differentiation" model proposed for RGLs [24]. While we observed some gradual RGL depletion over time, over 60% at 30 days and 30% at 60 days of Gli1$^{\#}$-RGL and Ascl1$^{\#}$-RGL clones retained at least one RGL after the initial RGL division (Figure 10C). Some Gli1$^{\#}$-RGL clones contained RGL(s) together with cells of both neuronal and astrocytic lineages, demonstrating RGL maintenance and multipotentiality at the single-cell level (Figure 10A). Meanwhile, most RGL-persisting Ascl1 clones contained cells of the neuronal lineage at various developmental stages, indicating multiple rounds of neurogenic self-renewal and maintenance at the single-cell level (Figure 10B).

To examine properties of labeled RGLs over time, we quantified RGL-retaining clones at 30 dpi according to cell type composition [23] and further constructed lineage trees from these clones (Figure 11A). Consistent with enhanced cell cycle re-entry at earlier time points, Ascl1$^{\#}$-RGLs divided more frequently over the 30 day period (Figure 11B). Compared to Ascl1$^{\#}$-RGLs, Gli1$^{\#}$-RGL clones displayed greater diversity of progeny with significantly higher percentages of multipotential differentiation (21 ± 10% vs. 1 ± 1%), astrocyte generation (26 ± 8% vs. 6 ± 4%) and RGL amplification (22 ± 8% vs. 6 ± 3%; Figure 12A). On the other hand, Ascl1$^{\#}$-RGL clones were significantly more neurogenic than Gli1$^{\#}$-RGL clones (86 ± 5% vs. 31 ± 8%; Figure 12A). Furthermore, Gli1$^{\#}$-RGLs exhibited more symmetric and astrogenic division than Ascl1$^{\#}$-RGLs, whereas Ascl1$^{\#}$-RGLs exhibit more neurogenic division (Figure 12B). Importantly, largely similar frequencies of self-renewal modes were observed at 3 and 30 dpi for both Gli1$^{\#}$-RGLs and

Ascl1$^{\#}$-RGLs (Figure 12B), indicating that RGLs labeled by these two approaches represent distinct stem cell populations, as opposed to one stem cell population that cycles among different states. Similar clone composition results were obtained at 60 dpi (Figure 12C). Together, these results support the model that Gli1$^{\#}$-RGLs represent multipotent neural stem cells, whereas Ascl1$^{\#}$-RGLs represent a distinct population of neuronal fate biased stem cells.

Figure 10 Maintenance of Gli1$^{\#}$-RGLs and Ascl1$^{\#}$-RGLs

(A) Sample confocal projection and single-section images of a multipotential Gli1$^{\#}$-RGL clone at 30 dpi. It contained two RGLs (via R-R division), with one generating IPCs of the neuronal lineage (1; R-N division) and another producing an astroglia (2; R-A division), thus exhibiting 3 different modes of self-renewal. Scale bars, 10 µm (5 µm for inserts).

(B) Sample confocal projection and single-section images of an Ascl1$^{\#}$-RGL clone that had undergone repeated neuronal divisions. Cell progeny from different developmental states include first produced mature neurons (4), then immature neurons (3), Tbr2^{+} IPCs (2) and the most recent IPC division from the RGL (1). Scale bars, 20 µm (5 µm for inserts).

(C) Quantification of RGL maintenance by the fraction of clones containing at least one RGL. Values represent mean ± SEM (n = 4-10 dentate gyri).

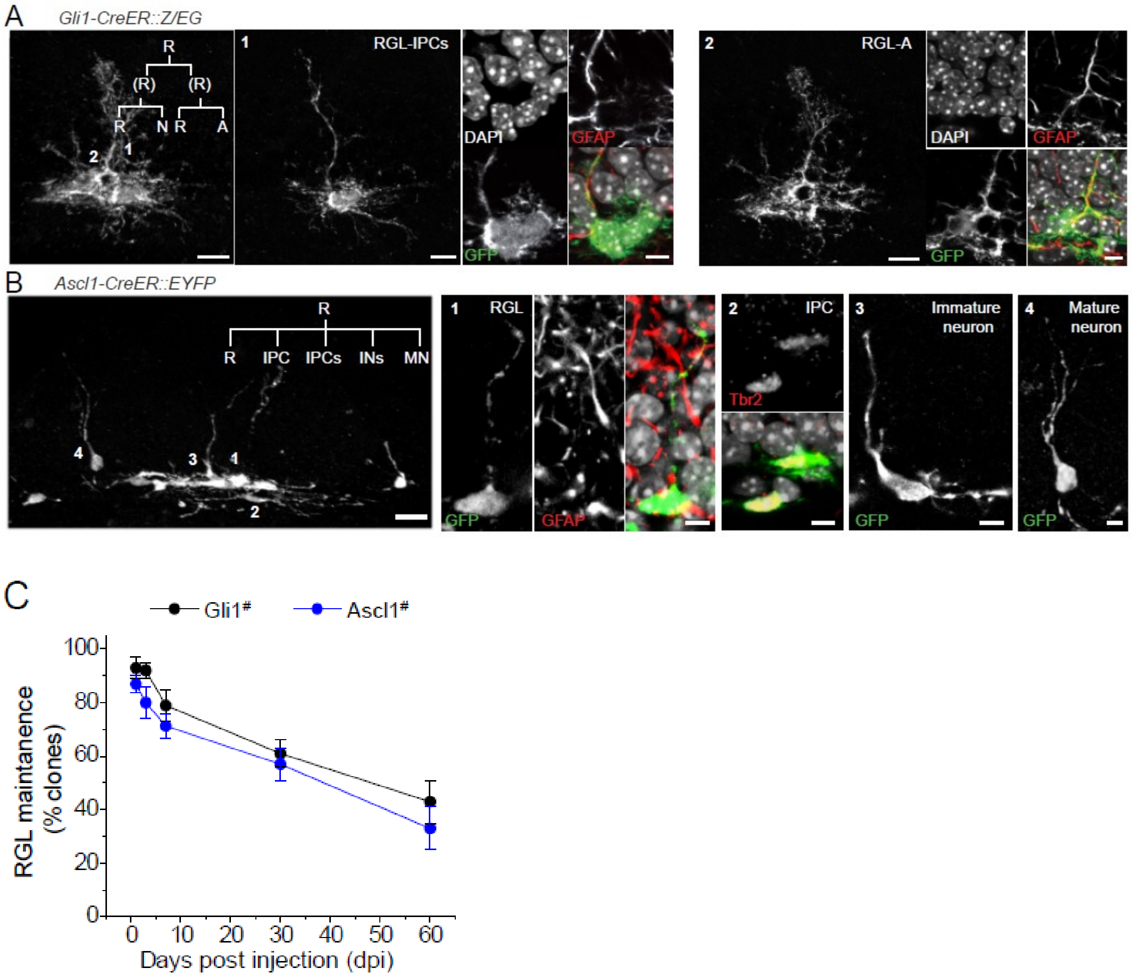
A
Gli1-CreER::Z/EG
R
(R)
(R)
R
N
R
A
2
1
1
RGL-IPCs
DAPI
GFAP
GFP
2
RGL-A
DAPI
GFAP
GFP
B
Ascl1-CreER::EYFP
R
R
IPC
IPCs
INs
MN
4
3
1
2
1
RGL
GFP
GFAP
2
IPC
Tbr2
3
Immature neuron
GFP
4
Mature neuron
GFP
C
Gli1#
Ascl1#
RGL maintanence (% clones)
100
80
60
40
20
0
0
10
20
30
40
50
60
Days post injection (dpi)

Figure 11 Long-term analyses of Gli1$^{\#}$-RGL and Ascl1$^{\#}$-RGL clones at 30 and 60 dpi

(A) List of observed lineage trees for Gli1$^{\#}$-RGLs and Ascl1$^{\#}$-RGLs at 30 dpi.

(B) Quantification of RGL-containing Ascl1$^{\#}$-RGL and Gli1$^{\#}$-RGL clone type at 30 dpi. Colors represent the same clone type as denoted in (A).

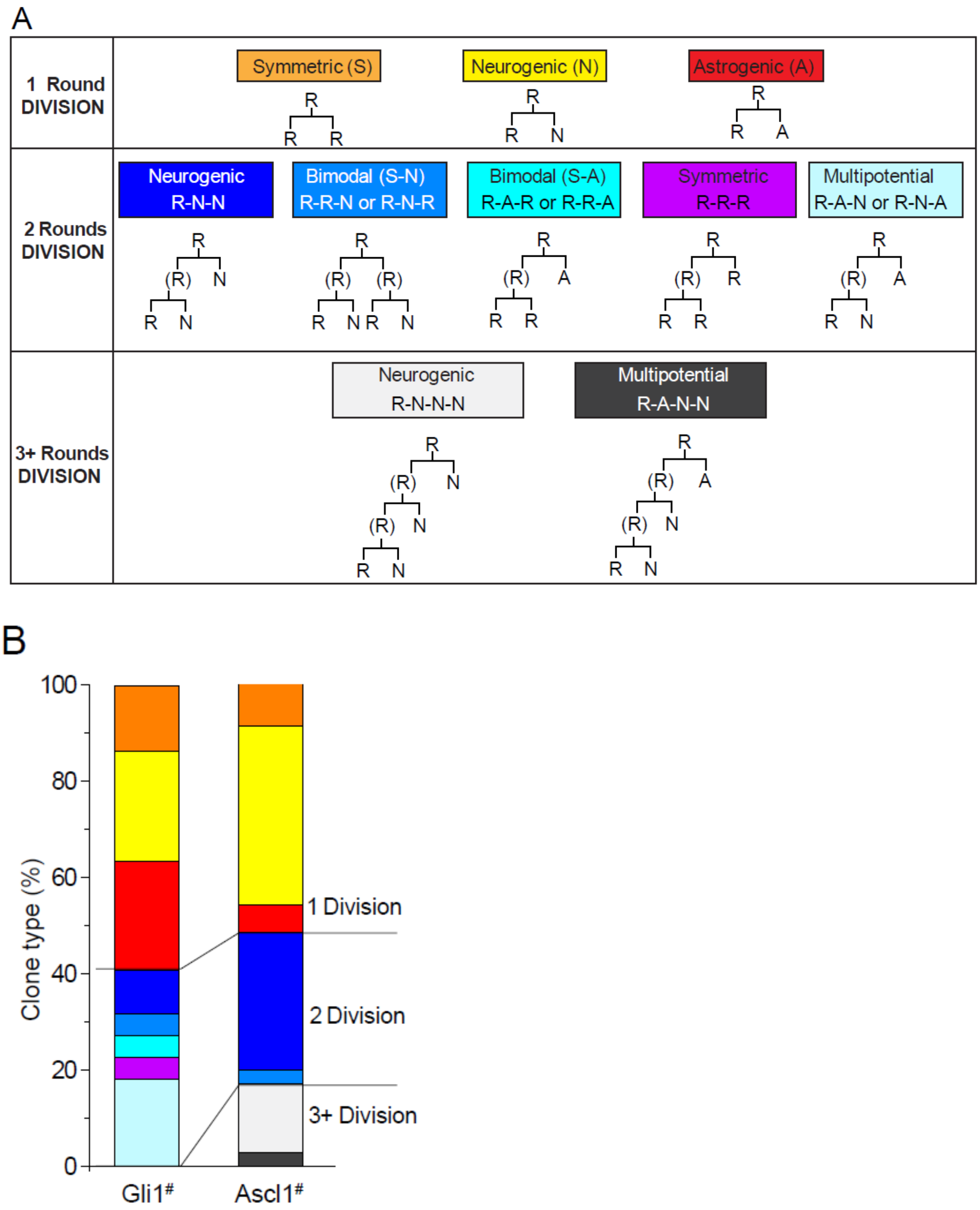
A
1 Round DIVISION
Symmetric (S)
R
R R
Neurogenic (N)
R
R N
Astrogenic (A)
R
R A
2 Rounds DIVISION
Neurogenic R-N-N
R
(R) N
R N
Bimodal (S-N) R-R-N or R-N-R
R
(R) (R)
R N R N
Bimodal (S-A) R-A-R or R-R-A
R
(R) A
R R
Symmetric R-R-R
R
(R) R
R R
Multipotential R-A-N or R-N-A
R
(R) A
R N
3+ Rounds DIVISION
Neurogenic R-N-N-N
R
(R) N
(R) N
R N
Multipotential R-A-N-N
R
(R) A
(R) N
R N
B
Clone type (%)
100
80
60
40
20
0
1 Division
2 Division
3+ Division
Gli1#
Ascl1#

Figure 12 Stem cell fate properties of multipotent Gli1$^{\#}$-RGLs and neuronal fate biased Ascl1$^{\#}$-RGLs

(A) Quantification of the frequency of clone composition types among RGL-retaining clones at 30 dpi for Ascl1$^{\#}$-RGLs ($n = 8$ dentate gyri) and Gli1$^{\#}$-RGLs ($n = 5$ dentate gyri). Values represent mean ± SEM. (**$p < 0.01$; *$p < 0.05$; Student’s t-test).

(B) Quantitative comparison of self-renewal fate choices made by Ascl1$^{\#}$-RGLs and Gli1$^{\#}$-RGLs at 3 dpi and over 30 days (30 dpi). Values represent mean ± SEM ($n = 5$-13 dentate gyri; *$p < 0.05$; n.s: $p > 0.1$; Student’s t-test).

(C) Quantification of the frequency of clone composition types among RGL-retaining clones at 60 dpi for Gli1$^{\#}$-RGLs ($n = 9$ dentate gyri) and Ascl1$^{\#}$-RGLs ($n = 7$ dentate gyri). Values represent mean ± SEM (*$p < 0.05$; n.s.: $p > 0.1$; Student’s t-test).

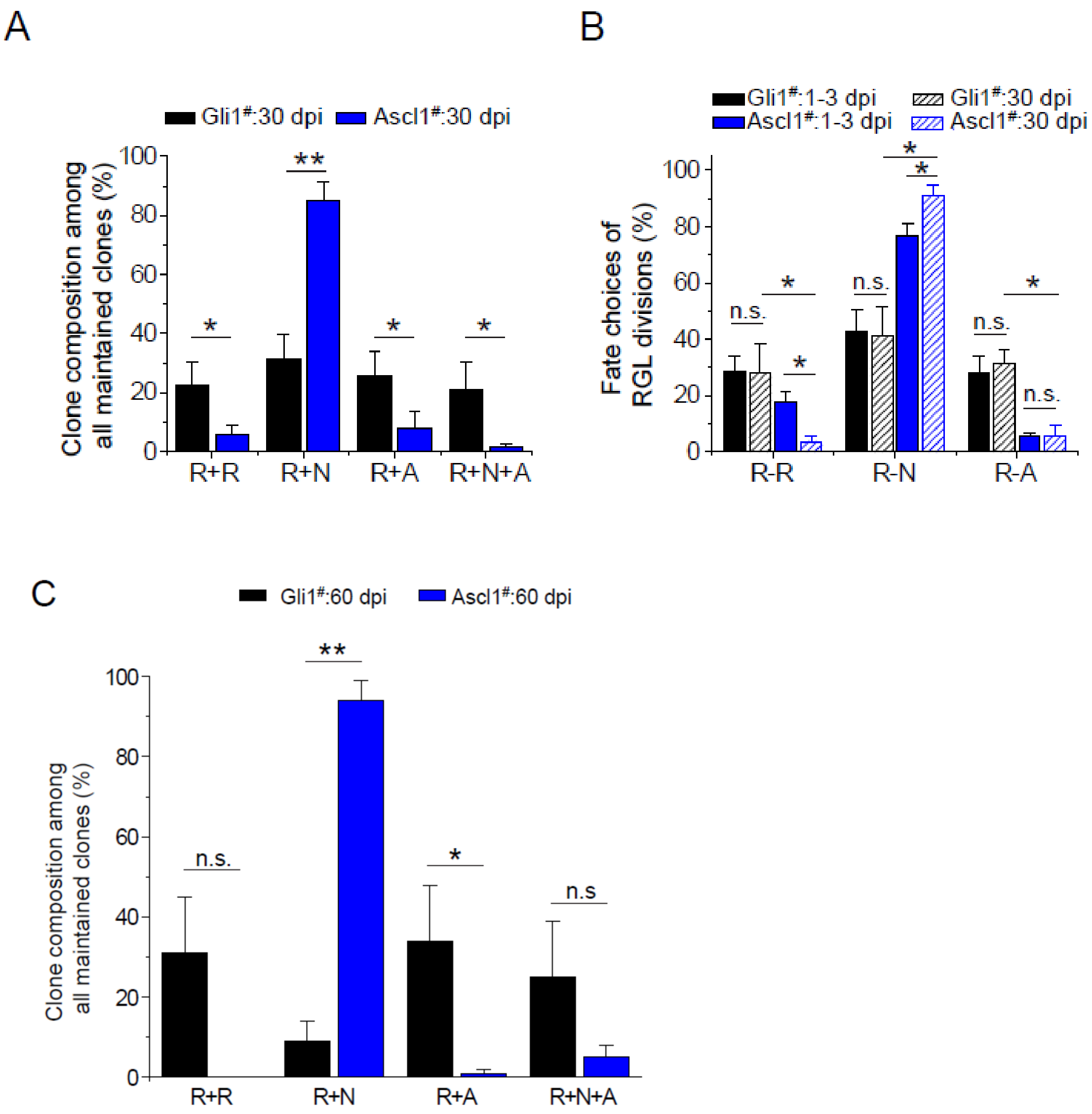
A
Gli1$^{\#}$:30 dpi
Ascl1$^{\#}$:30 dpi
Clone composition among all maintained clones (%)
0
20
40
60
80
100
*
**
*
*
R+R
R+N
R+A
R+N+A
B
Gli1$^{\#}$:1-3 dpi
Ascl1$^{\#}$:1-3 dpi
Gli1$^{\#}$:30 dpi
Ascl1$^{\#}$:30 dpi
Fate choices of RGL divisions (%)
0
20
40
60
80
100
n.s.
*
*
n.s.
*
*
n.s.
*
n.s.
R-R
R-N
R-A
C
Gli1$^{\#}$:60 dpi
Ascl1$^{\#}$:60 dpi
Clone composition among all maintained clones (%)
0
20
40
60
80
100
n.s.
**
*
n.s
R+R
R+N
R+A
R+N+A

3.5 Computational Assessment of Different States and Discrete Neural Stem Cell Populations

To further assess our model, we applied a computational approach, which accounted for differences in the activation kinetics of stem cells[6, 57], to quantitatively describe the behavior of Nestin$^{\#}$-RGLs, Gli1$^{\#}$-RGLs and Ascl1$^{\#}$-RGLs over an extended period of time (Figure 13A; See Methods). Raw clonal lineage-tracing data from different time points were analyzed to infer the initial activation time after labeling (T_{entry}; Figures 13B, 14A-C), kinetics of subsequent cell cycle re-entry (T_c; Figures 13C, 14D-F), and cell fate decisions (Figures 13D, 14G-I). Our analyses indicated that Gli1$^{\#}$-RGLs and Ascl1$^{\#}$-RGLs rapidly entered cell cycle with an average initial activation time of 0.78 ± 0.02 and 0.35 ± 0.04 days, respectively, while that for Nestin$^{\#}$-RGLs was 23 ± 3 days (Figures 13B, 15). Despite the initial activation time offset, Nestin$^{\#}$-RGLs and Gli1$^{\#}$-RGLs exhibited similar cell cycle re-entry time (T_c), which was significantly longer than that of Ascl1$^{\#}$-RGLs (Figure 13C). Furthermore, Nestin$^{\#}$-RGLs and Gli1$^{\#}$-RGLs displayed very similar probabilities of various self-renewal division modes, which were also significantly different from those of Ascl1$^{\#}$-RGLs (Figure 13D). Altogether, these results are consistent with our model that Nestin$^{\#}$-RGLs and Gli1$^{\#}$-RGLs represent a single equipotent stem cell population labeled at different states in the cell cycle, whereas Ascl1$^{\#}$-RGLs represent a distinct population.

We further compared the average content of RGL-containing clones labeled by three different approaches as a function of time (Figure 16). To compensate for the initial activation time offset, the average content per RGL-containing clone for Nestin$^{\#}$-RGLs at 30, 60 and 120 dpi were compared to Gli1$^{\#}$-RGLs and Ascl1$^{\#}$-RGLs at 7, 30 and 60 dpi, respectively. Strikingly, the composition of Nestin$^{\#}$ and Gli1$^{\#}$ clones mirrored one another over time (Figure 16). In contrast, Ascl1$^{\#}$ clones contained more cells of the neuronal lineage and fewer cells of the astroglial lineage (Figure 16). These observations further support the model that Gli1$^{\#}$ marks the same stochastic, multipotent quiescent RGL as Nestin$^{\#}$ but in a pre-activation state, whereas Ascl1$^{\#}$ labels a discrete RGL population fate biased for neurogenesis.

Figure 13 Stem cell kinetics revealed by a computational approach

(A-D) Neural stem cell activation kinetics and basic characteristics derived from computational analysis of Nestin$^{\#}$-RGL, Gli1$^{\#}$-RGL and Ascl1$^{\#}$-RGL clonal lineage-tracing data. Shown in (A) is a schematic depicting the life cycle of adult hippocampal RGL neural stem cells with following key parameters: time to first division upon initial labeling (T_{entry}), cell cycle re-entry time (T_c), and fate choices probabilities including astrocytic (P_{RA}), symmetric (P_{RR}), and neuronal (P_{RN}) self-renewal modes. Also shown are summaries of mean T_{entry} (B), T_C (C) and fate choices (D) as inferred from computational modeling and fit to experimental data between 1-30 dpi.

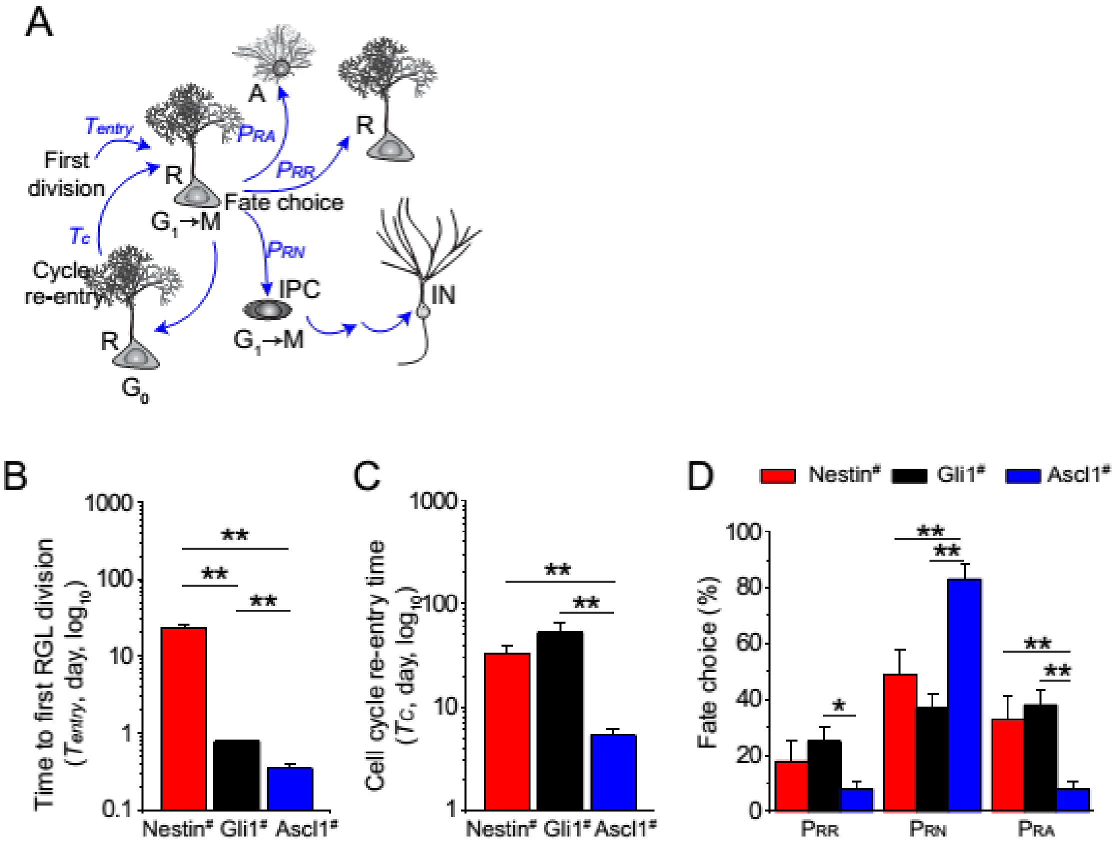
A
A
R
T_{entry}
P_{RA}
First division
R
P_{RR}
Fate choice
$G_1 \rightarrow M$
T_c
P_{RN}
Cycle re-entry
IPC
IN
R
$G_1 \rightarrow M$
G_0
B
Time to first RGL division (T_{entry}, day, $\log_{10}$)
1000
100
10
1
0.1
**
**
**
Nestin# Gli1# Ascl1#
C
Cell cycle re-entry time (T_C, day, $\log_{10}$)
1000
100
10
1
**
**
Nestin# Gli1# Ascl1#
D
Nestin# Gli1# Ascl1#
Fate choice (%)
100
80
60
40
20
0
*
**
**
**
**
PRR
PRN
PRA

Figure 14 Computational assessment of RGL properties

(A-C) Plots of RGL quiescence as a function of time. Activation kinetics (Figure 12B) are inferred from the exponential rate of decay for Nestin$^{\#}$-RGLs (A), Gli1$^{\#}$-RGLs (B), and Ascl1$^{\#}$-RGL (C). Note the time scale difference.

(D-F) Plots of the fraction of RGLs that divided only once as a function of time. Cell cycle re-entry time (T_c, Figure 12C) reflects the decay rate following the peak for Nestin$^{\#}$-RGLs (G), Gli1$^{\#}$-RGLs (H) and Ascl1$^{\#}$-RGLs (I). Note the time scale difference.

(G-I) Plots of least squares fit of modeling results to the experimentally observed frequency of clones within Nestin$^{\#}$-RGL (D), Gli1$^{\#}$-RGL (E) and Ascl1$^{\#}$-RGL (F) lineage-tracing.

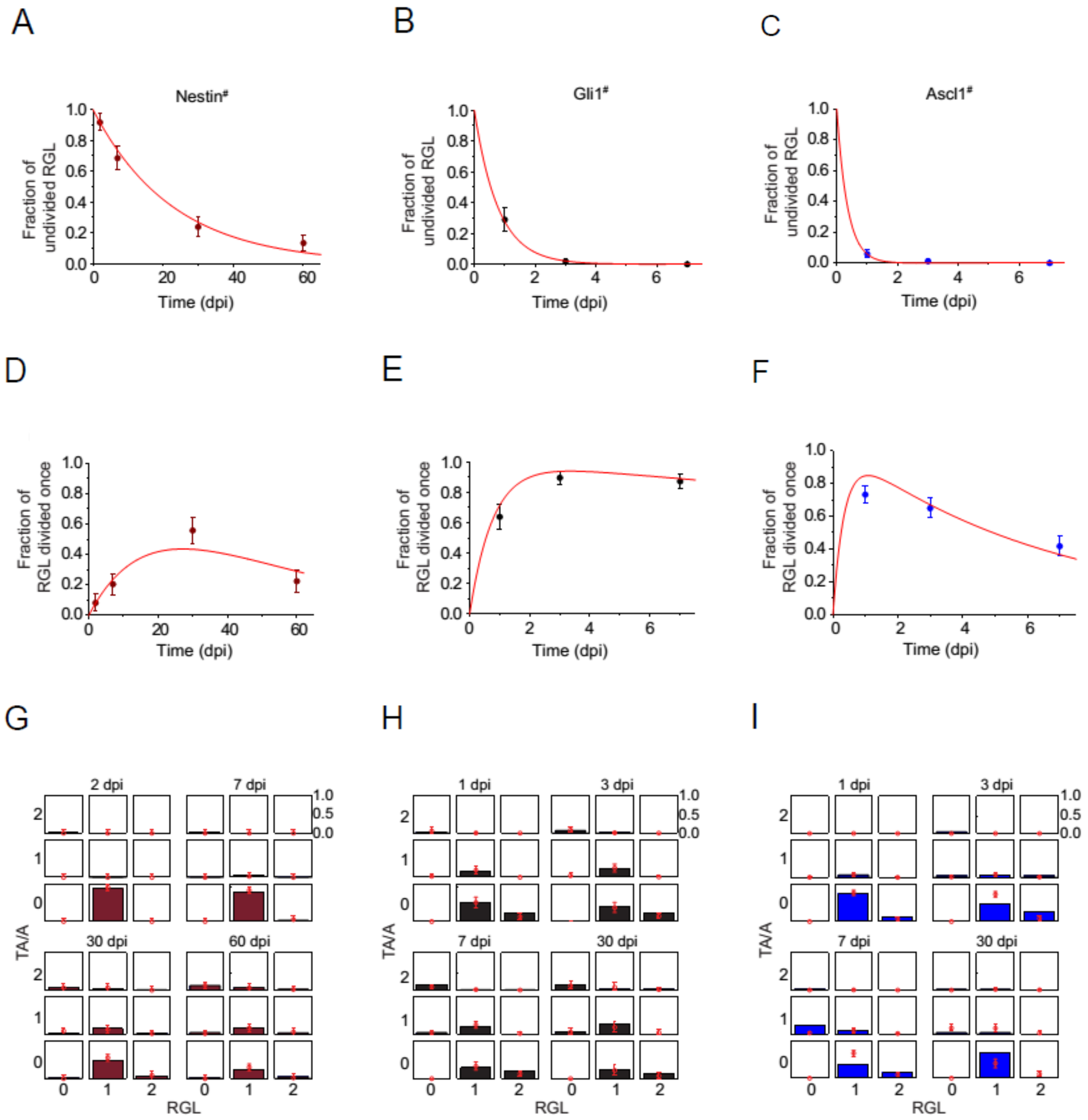
A
Nestin#
Fraction of undivided RGL
1.0
0.8
0.6
0.4
0.2
0.0
0
20
40
60
Time (dpi)
B
Gli1#
Fraction of undivided RGL
0
2
4
6
Time (dpi)
C
Ascl1#
Fraction of undivided RGL
Time (dpi)
D
Fraction of RGL divided once
Time (dpi)
E
Fraction of RGL divided once
Time (dpi)
F
Fraction of RGL divided once
Time (dpi)
G
2 dpi
7 dpi
30 dpi
60 dpi
TA/A
RGL
0
1
2
1.0
0.5
0.0
H
1 dpi
3 dpi
7 dpi
30 dpi
TA/A
RGL
I
1 dpi
3 dpi
7 dpi
30 dpi
TA/A
RGL

Figure 15 Validation of computational models

(A) Fraction of Nestin$^{\#}$-RGL clones with the specified number of RGL and astroglial lineage (TA/A) at different time points (stars) and model prediction (dashes). Values represent mean ± SEM.

(B) Fraction of Nestin$^{\#}$-RGL clones that retain at least one RGL at specified time points and model prediction.

(C) Fate choice probabilities obtained by fitting the solution of the master equation to the experimentally observed Nestin$^{\#}$-RGL clone size distributions and fate choice probabilities deduced from lineage-tracing data. RR: RGL-RGL division, RI: RGL-IPC division, RA: RGL-astroglia division, II: IPC-IPC division, AA: astroglia-astroglia division, IA: IPC-astrocyte division.

(D) Fraction of Gli1$^{\#}$-RGL clones with the specified number of RGL and astroglial lineage (TA/A) at different time points and model prediction.

(E) Fraction of Ascl1$^{\#}$-RGL clones with the specified number of RGL and astroglial lineage (TA/A) at different time points and model prediction.

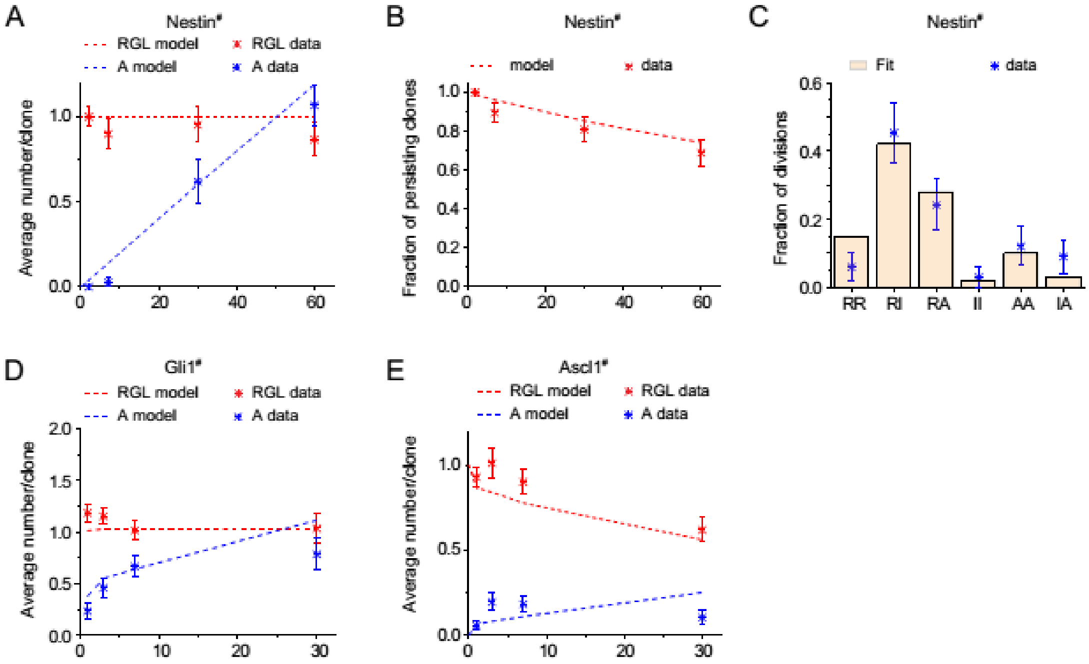
A
Nestin#
RGL model
RGL data
A model
A data
Average number/clone
0.0
0.5
1.0
0
20
40
60
B
Nestin#
model
data
Fraction of persisting clones
0.0
0.2
0.4
0.6
0.8
1.0
0
20
40
60
C
Nestin#
Fit
data
Fraction of divisions
0.0
0.2
0.4
0.6
RR
RI
RA
II
AA
IA
D
Gli1#
RGL model
RGL data
A model
A data
Average number/clone
0.0
0.5
1.0
1.5
2.0
0
10
20
30
E
Ascl1#
RGL model
RGL data
A model
A data
Average number/clone
0.0
0.5
1.0
0
10
20
30

Figure 16 Statistical ensembles of RGL clones

(A) Statistical ensembles of RGL clones representing the average content of different progeny types per clone as a function of time. The neuronal lineages include IPCs, immature neurons (IN) and mature neurons (MN), and the astroglial lineages include transition astroglia (TA) and astrocytes (A). Note the time scale difference (x-axis) from Nestin$^{\#}$-RGLs to Gli1$^{\#}$-RGLs and Ascl1$^{\#}$-RGLs, reflecting distinct T_{entry}.

A

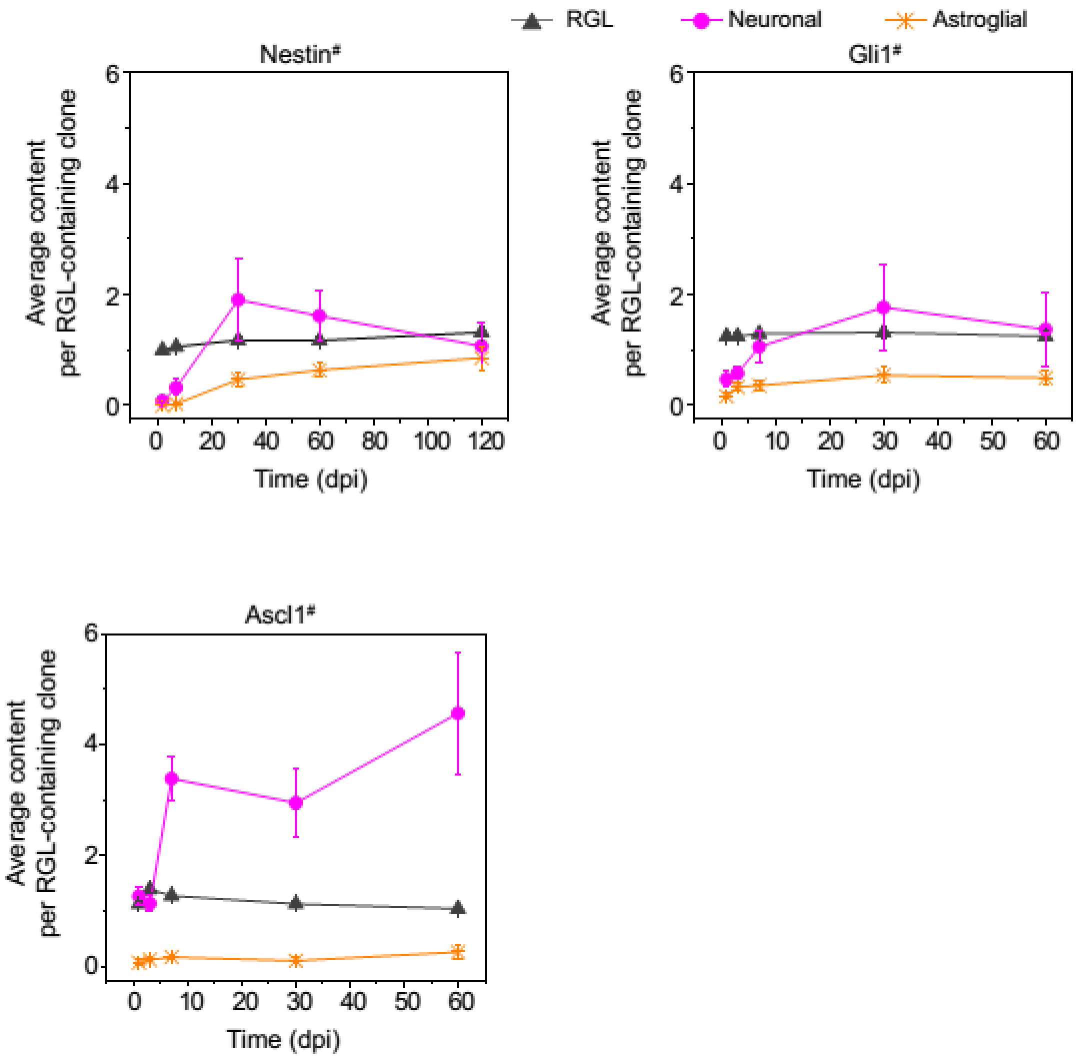
RGL
Neuronal
Astroglial
Nestin#
Gli1#
Ascl1#
Average content per RGL-containing clone
0
2
4
6
0
20
40
60
80
100
120
0
10
20
30
40
50
60
Time (dpi)

3.6 Plasticity of Different RGLs after Injury

As both lineage-tracing and computational analyses indicated that Gli1$^{\#}$-RGLs/Nestin$^{\#}$-RGLs and Ascl1$^{\#}$-RGLs exist as distinct stem cell populations under physiological conditions, we next examined whether their intrinsic properties are fixed or could be influenced by the extrinsic environment in the adult neurogenic niche. Stem cells in various somatic compartments are differentially utilized under physiological or pathological conditions [7]. In the adult brain, quiescent precursor cells are activated to restore depleted IPCs and neuroblasts after the Cytosine Arabinofuranoside (AraC) treatment to kill dividing cells[43, 61]. It remains unknown, however, whether and how quiescent RGL stem cell behavior changes during injury-induced regeneration. We labeled Gli1$^{\#}$-RGLs at the clonal level (Table 1), waited for the initial division to complete to avoid killing them, and then infused AraC for 4 days (Figure 17A). EdU was injected during the AraC administration period to monitor efficacy of proliferating cell depletion (Figure 17A). After the 7 day chase, EdU^{+} cells were largely absent from the SGZ in the AraC group, but were present in those without AraC treatment (Figure 17B). GFAP immunohistology further revealed reactive gliosis after AraC treatment within the dentate gyrus, demonstrating a local injury response (Figure 17C).

Upon confirming the AraC model, we analyzed RGL-containing clones 7 days after injury. Remarkably, nearly all Gli1$^{\#}$-RGLs became activated in response to AraC injury and exhibited repeated self-renewal and IPC generation, resembling Ascl1$^{\#}$-RGLs under physiological conditions (Figures 18A and C). To define Gli1$^{\#}$-RGL behavior more precisely in response to injury, we again constructed lineage trees (Figure 19A). Gli1$^{\#}$-RGL cell cycle re-entry frequency after injury was significantly increased to a level similar to Ascl1$^{\#}$-RGLs under basal conditions (Figure 18C). Quantification of self-renewal mode indicates that neurogenic and symmetric divisions of Gli1$^{\#}$-RGLs increased in response to injury, with a corresponding decrease in astrogenesis (Figures 18D and 19B). For Gli1$^{\#}$-RGLs in the sham control group without AraC infusion, the self-renewal mode was largely similar to clones under basal conditions at 7 dpi, further validating the persistence of intrinsic Gli1$^{\#}$-RGL properties (Figure 19C). Together, these results showed that Gli1$^{\#}$-RGLs after AraC injury phenocopy basal Ascl1$^{\#}$-RGL characteristics. Likewise, Nestin$^{\#}$-RGLs after injury exhibited similar properties as Gli1$^{\#}$-RGLs after injury and Ascl1$^{\#}$-RGLs under basal conditions (Figure 20). These results provide additional support of our model that Nestin$^{\#}$-RGLs and Gli1$^{\#}$-RGLs represent the same population of quiescent neural stem cells and further showed that the stochastic behavior of largely quiescent RGLs can be altered in response to changes in the extrinsic environment.

Finally, we examined Ascl1$^{\#}$-RGLs after the same injury paradigm. The number of labeled RGL-containing clones were significant reduced right after AraC treatment (Figure 21A), suggesting that many proliferative Ascl1$^{\#}$-RGLs were depleted upon this injury. We followed the fate of remaining Ascl1$^{\#}$-RGLs at 7 dpi and found that these RGLs exhibited increased symmetric cell division at the expense of neurogenic self-renewal (Figure 18D). Therefore, upon injury Ascl1$^{\#}$-RGLs exhibit different properties than those under basal conditions and different than the injury response of Nestin$^{\#}$-RGLs and Gli1$^{\#}$-RGLs. Together, these results revealed remarkable plasticity of different RGL populations and their differential contribution to cell genesis under both basal and injury conditions.

Figure 17 Gli1$^{\#}$-RGL and Ascl1$^{\#}$-RGL AraC-induced injury experimental paradigm

(A) Schematic illustration of experimental paradigms.

(B-C) Sample confocal images of EdU staining (B) and GFAP immunohistology (C) at 7 days after completion of AraC treatment. Scale bars: 100 µm (20 µm for inserts). For GFAP images, samples were processed in parallel and acquired with same confocal settings for control and AraC groups

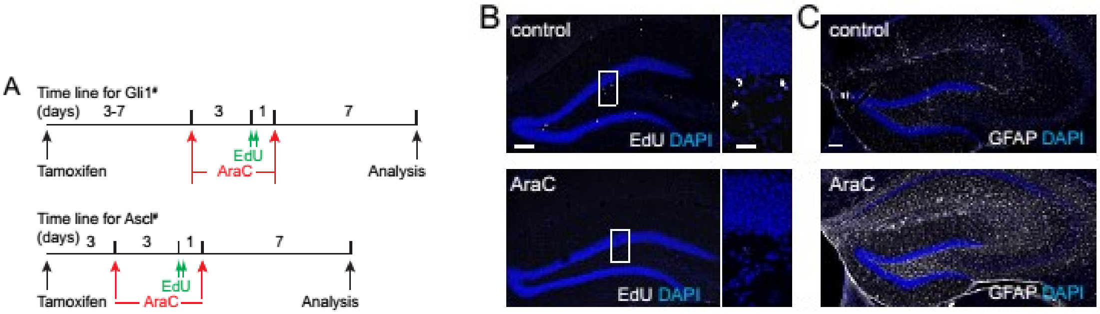
A
Time line for Gli1*
(days)
3-7
3
1
7
Tamoxifen
EdU
AraC
Analysis
Time line for Ascl*
(days)
3
3
1
7
Tamoxifen
EdU
AraC
Analysis
B
control
EdU DAPI
AraC
EdU DAPI
C
control
GFAP DAPI
AraC
GFAP DAPI

Figure 18 Plasticity of RGL behavior after AraC-induced injury

(A-B) Sample confocal projection and single-section images of Gli1$^{\#}$-RGL (A) and Ascl1$^{\#}$-RGL (B) 7 days after the stop of AraC treatment. Shown are examples of the Gli1$^{\#}$-RGL that generated multiple cells of the neuronal lineage (A) and the Ascl1$^{\#}$-RGL that underwent symmetric cell division (B). Lineage trees indicating self-renewal modes are shown next to the projection images. Scale bars, 10 μm (5 μm for inserts).

(C-D) Quantification of percentages of RGL clones that divided (C, left) and that re-entered cell cycle (C, right), and division modes (D) under different conditions. Values represent mean ± SEM (n = 5-6; *p < 0.01, **p < 0.001, n.s : p > 0.1; Student's t-test).

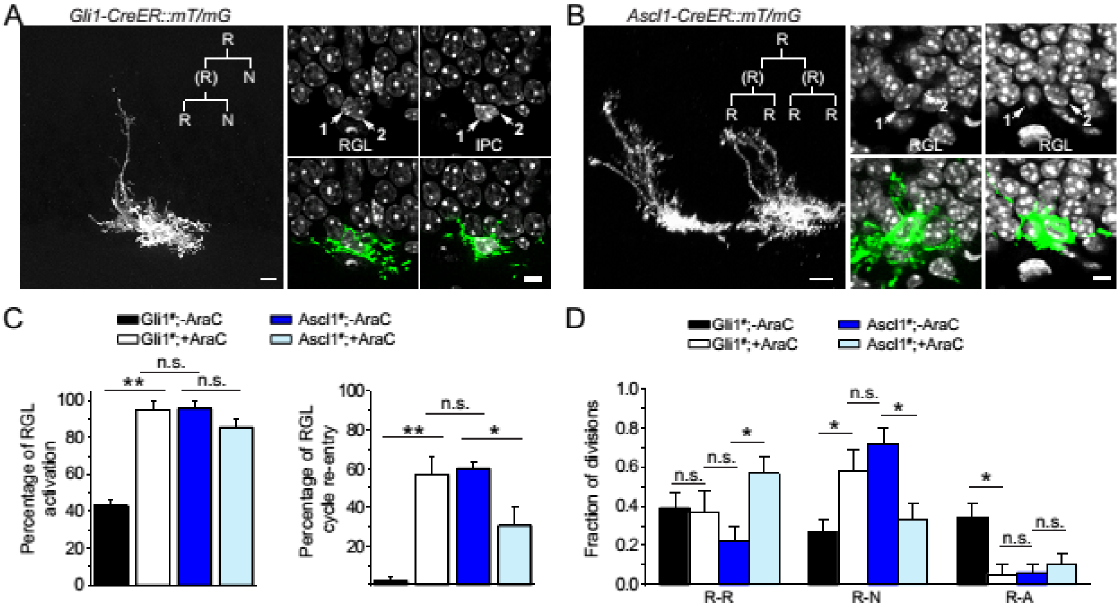
A
Gli1-CreER::mT/mG
R
(R)
N
R
N
1
2
RGL
1
2
IPC
B
Ascl1-CreER::mT/mG
R
(R)
(R)
R
R
R
R
1
2
RGL
1
2
RGL
C
Gli1*;-AraC
Gli1*;+AraC
Ascl1*;-AraC
Ascl1*;+AraC
**
n.s.
n.s.
Percentage of RGL activation
0
20
40
60
80
100
Percentage of RGL cycle re-entry
20
40
60
80
100
**
n.s.
*
D
Gli1*;-AraC
Gli1*;+AraC
Ascl1*;-AraC
Ascl1*;+AraC
Fraction of divisions
0.0
0.2
0.4
0.6
0.8
1.0
n.s.
n.s.
*
*
n.s.
*
*
n.s.
n.s.
R-R
R-N
R-A

Figure 19 Changes of Gli1$^{\#}$-RGL and Ascl1$^{\#}$-RGL behavior upon AraC-induced injury

(A-B) List of observed lineage trees for Gli1$^{\#}$-RGLs and Ascl1$^{\#}$-RGLs (A) and quantification of RGL-containing clone types (B).

(C) Summary of fate choices among controls for AraC injury. Fraction of divisions are consistent between normal and AraC sham conditions for both Gli1$^{\#}$-RGLs and Ascl1-RGLs. Values represent mean ± SEM (n = 3-9 dentate gyri).

A

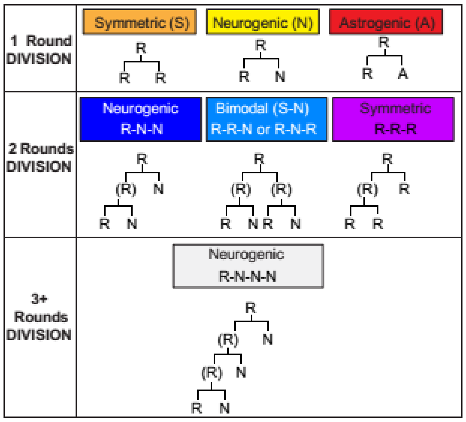
1 Round DIVISION
Symmetric (S)
R
R R
Neurogenic (N)
R
R N
Astrogenic (A)
R
R A
2 Rounds DIVISION
Neurogenic R-N-N
R
(R) N
R N
Bimodal (S-N) R-R-N or R-N-R
R
(R) (R)
R N R N
Symmetric R-R-R
R
(R) R
R R
3+ Rounds DIVISION
Neurogenic R-N-N-N
R
(R) N
(R) N
R N

B

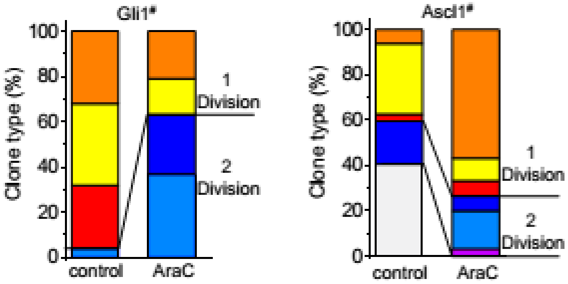
Gli1#
Clone type (%)
100
80
60
40
20
0
control
AraC
1 Division
2 Division
Ascl1#
Clone type (%)
100
80
60
40
20
0
control
AraC
1 Division
2 Division

C

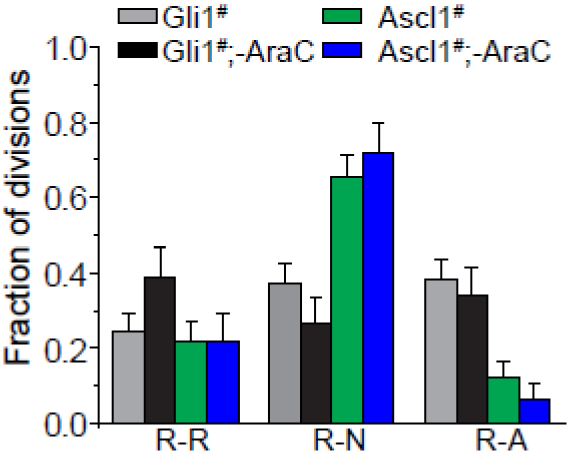
Gli1#
Gli1#;-AraC
Ascl1#
Ascl1#;-AraC
Fraction of divisions
1.0
0.8
0.6
0.4
0.2
0.0
R-R
R-N
R-A

Figure 20 Nestin$^{\#}$-RGL behavior after AraC treatment

(A) Schematic illustration of experimental paradigm.

(B) Sample confocal projection and single-section images of GFP-labeled Nestin$^{\#}$-RGL clones 7 days after the stop of AraC treatment. Shown are examples of Nestin$^{\#}$-RGLs that generated multiple cells of the neuronal lineage. Lineage trees indicating self-renewal modes are shown next to the projection images. Arrows point to cells within the clone. Scale bars, 10 μm (5 μm for inserts).

(C-D) Summary of quantification of percentages of RGL clones that divided (C, left) and that re-entered cell cycle (C, right), and activated RGL clones that generate new IPCs (D, left), as well as summary of activated RGL clonal fate decisions (D, right) after AraC treatment. The responses of Gli1$^{\#}$-RGLs to AraC are re-plotted (see Figure 6) for comparison (D). Values represent mean ± SEM (n = 4 dentate gyri; *$p < 0.05$, n.s.: $p > 0.1$; Student's t-test)

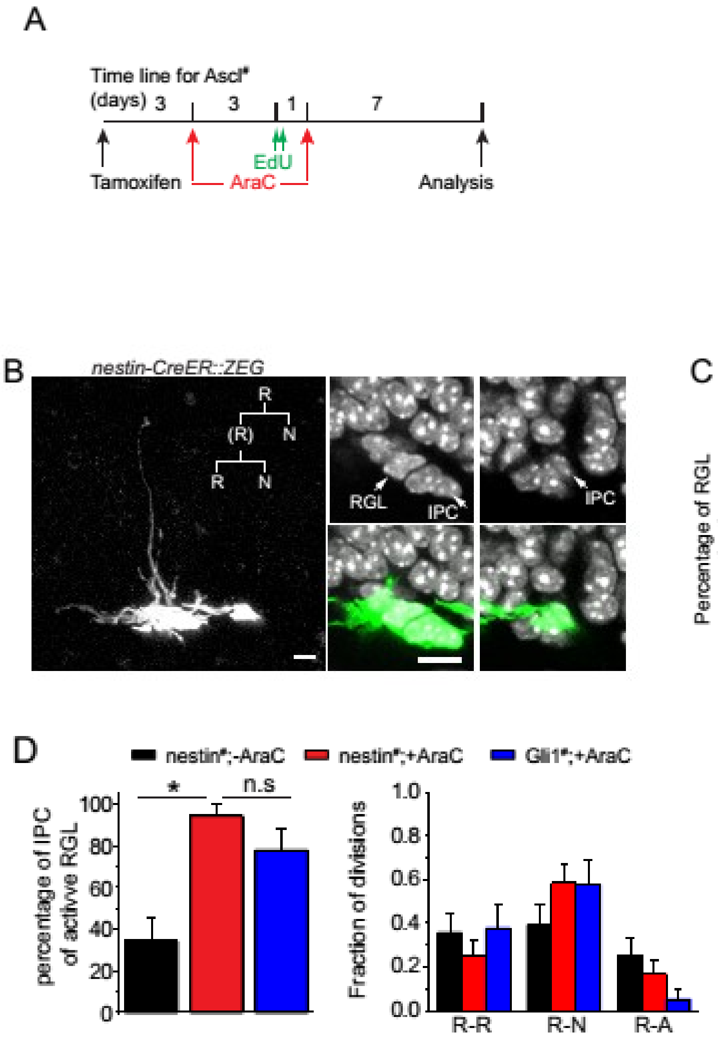
A
Time line for Ascl*
(days) 3
3
1
7
Tamoxifen
EdU
AraC
Analysis
B
nestin-CreER::ZEG
R
(R)
N
R
N
RGL
IPC
IPC
C
nestin*;-AraC
nestin*;+AraC
Percentage of RGL activation
Percentage of RGL cycle re-entry
0
20
40
60
80
100
*
*
D
nestin*;-AraC
nestin*;+AraC
Gli1*;+AraC
percentage of IPC of activve RGL
*
n.s
Fraction of divisions
0.0
0.2
0.4
0.6
0.8
1.0
R-R
R-N
R-A

Figure 21 Reduced number of Ascl1#-RGL containing clones in AraC treatment

(A) Quantification of the number of Ascl1$^{\#}$ RGL-containing clones after AraC injury.

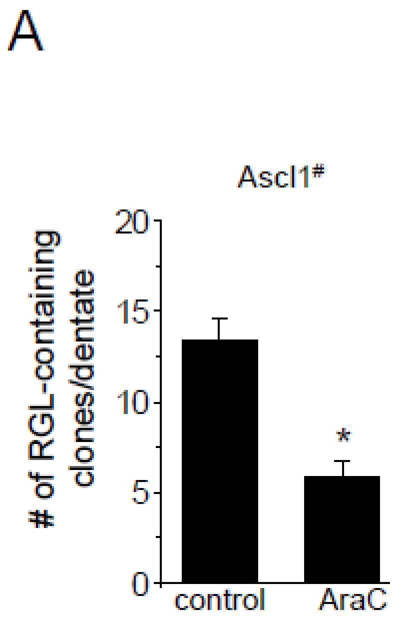
A
Ascl1#
# of RGL-containing clones/dentate
20
15
10
5
0
*
control
AraC

Figure 23 Cartoon summary depicting different states and discrete populations of RGL neural stem cell populations in the young adult mouse hippocampus.

Nestin$^{\#}$ and Gli1$^{\#}$ mark the same population of self-renewing, multipotent and quiescent RGL neural stem cells at distinct states. Nestin$^{\#}$ labels RGLs during a more quiescent state, while Gli1$^{\#}$ marks RGLs at a pre-activation state hours before division. On the other hand, Ascl1$^{\#}$ labels a distinct population of self-renewing, neuronal fate biased and more proliferative RGL neural stem cells in the same region of the hippocampus under physiological conditions. Noted the duration until first RGL division after labeling (T_{entry}) for lineage-tracing and the duration of cell cycle re-entry (T_C). Upon AraC injury, Gli1$^{\#}$-RGLs and Nestin$^{\#}$-RGLs behave similarly to Ascl1$^{\#}$-RGLs under physiological conditions, whereas Ascl1$^{\#}$-RGLs also change their properties to primarily symmetric division. Strength of arrows denotes relative probability of fate choices.

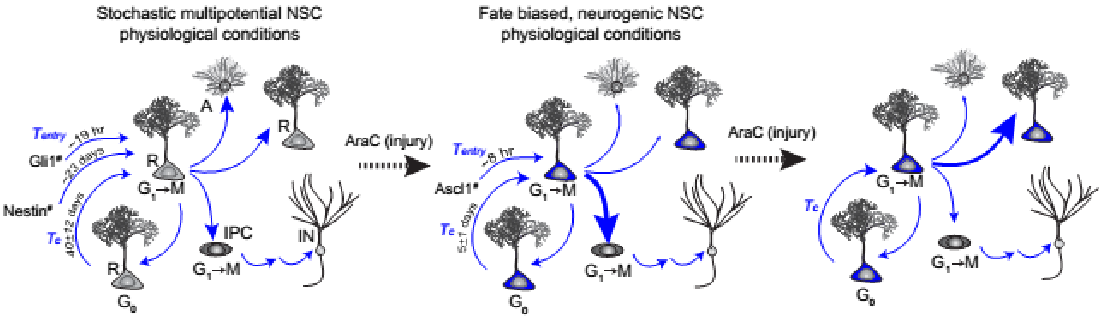
Stochastic multipotential NSC physiological conditions
T_{entry}
~19 hr
Gli1*
~23 days
Nestin*
T_c
40±12 days
R
A
R
$G_1 \rightarrow M$
R
G_0
IPC
$G_1 \rightarrow M$
IN
AraC (injury)
Fate biased, neurogenic NSC physiological conditions
T_{entry}
~8 hr
Ascl1*
T_c
5±1 days
$G_1 \rightarrow M$
G_0
$G_1 \rightarrow M$
AraC (injury)
T_c
$G_1 \rightarrow M$
G_0
$G_1 \rightarrow M$

4 Discussion

Stem cells often display complex behaviors over time due to their dynamic nature. Using adult neural stem cells in the hippocampus as an in vivo model system, we combined clonal lineage-tracing with computational approaches to deconstruct and resolve stem cell heterogeneity and plasticity. Unexpectedly, two of our three RGL-labeling strategies birthdate adult neural stem cell division and therefore allow, for the first time, direct quantification of their basic properties in vivo, including cell cycle kinetics, self-renewal mode, cell cycle exit and maintenance after division. Our study revealed the co-existence of both stochastic, multipotent neural stem cells and a distinct, previously unrecognized population of neuronal fate biased neural stem cells that exhibit similar morphology and location and act in parallel under physiological conditions in the adult hippocampus (Figure 23). In addition, we demonstrated that apparent stem cell heterogeneity may reflect the observation of different states of the same stem cell population. Finally, we revealed the plastic nature of different neural stem cell populations in response to anti-mitotic injury, including a transition from stochastic to fate biased stem cell behavior. These findings not only provide novel insight into the biology of neural stem cells and their intrinsic properties and plasticity in the adult mammalian brain, but also suggest an integrative approach to deconstruct and resolve stem cell complexity that may have broad applicability to the general stem cell field.

Transient Stem Cell States and Discrete Stem Cell Populations

Stem cells exhibit cell-to-cell phenotypic variability in the cell cycle status[62, 63], oscillations in gene transcription[64, 65], and contributions to tissue plasticity [7]. Determining which properties define stem cells or modulate their behavior remains a general challenge for the stem cell field [66]. Heterogeneity may occur within a single stem cell population transitioning through different transient states[67, 68]; in contrast, differences in stem cell properties that persist over time are indicative of distinct stem cell populations. While tissue architecture, distinct niches, or invariant behavior enable segregation of stem cells into definable populations in some systems[69-71], in many other systems it remains unclear whether discrete stem cell populations that share certain linage potentials co-exist within the same niche[8, 20, 21, 72-74].

Many stem cells exhibit cycles of activation, fate specification and then return to quiescence. Commonly used approaches for lineage-tracing, including genetic and nucleotide analog labeling, target precursors at particular stages of these cycles; therefore, short-term analysis may result in an incomplete picture of stem cell behavior. Quantitative determination of cell cycle kinetics and lineage production over prolonged period of time can overcome this limitation and account for differences in stem cell states upon labeling [1]. Our retrospective computational analysis of clonal data provides an illustration of this principle. Specifically, in the adult mouse dentate gyrus Nestin$^{\#}$-RGLs and Gli1$^{\#}$-RGLs represent the same stochastic multipotential stem cell population labeled in quiescent and pre-activation states, respectively (Figure 23). This conclusion was drawn from similar cell cycle re-entry time, cell fate probabilities under both basal conditions and upon injury, and kinetics of lineage production between the two labeling paradigms after controlling for differences in the time to first division (Figures 13, 14 and 15; See Theory in Methods). As the time to first cell cycle entry (T_{entry}) of labeled Gli1$^{\#}$-RGLs differs significantly from their cell cycle time (T_c), our results indicate that the behavior of stem cells shortly after genetic labeling may not reflect fundamental characteristics of the cell population to which they belong. Instead, consistent characteristics over multiple rounds of self-renewal more accurately reflect intrinsic properties of a particular stem cell population. These considerations are paramount in properly interpreting stem cell identity. For example, analysis of initial proliferation alone could lead to the mis-interpretation that Gli1$^{\#}$-RGLs and Ascl1$^{\#}$-RGLs represent the same neural stem cell population that is distinct from Nestin$^{\#}$-RGLs. In addition, short-term examination of Ascl1$^{\#}$-RGL cell cycle re-entry time would indicate an “active” stem cell population instead of a dynamic population that switches to quiescence after divisions. Our results suggest that the term “quiescent” or “active” better describes different states of stem cells, but may be inadequate to fully distinguish between discrete populations of stem cells. Overall, our study demonstrates a general strategy to define stem cell identity by accounting for potential differences in the state of originally labeled cells.

Neural Stem Cell Relationships in the Adult Hippocampus

A common theme of ongoing cell genesis is the hierarchical organization of co-existent stem cell populations in vivo, including adult dentate gyrus and subventricular zone on the basis of population fate-mapping studies[8, 20, 21, 23, 24, 37, 38, 72-74]. Studies of proliferation kinetics in hematopoiesis [75] and muscle [76] show evidence for heterogeneity at the apex of the stem cell compartment, with “dormant” cells primed for survival and more active but slow-cycling cells biased towards differentiation and loss. Recent lineage-tracing studies based on genetic labeling and live-imaging of the intestinal crypt[68], hair follicle [77], and germline[78] have provided evidence that stem cells may transfer reversibly between these compartments, adjusting their bias, and changing levels of gene expression in response to signals from the niche. In somatic tissues it is common to predominantly employ one precursor population for physiological functions with another cell population for pathological conditions. In many damaged tissues, a “reserve” cell population contributes to repair despite not acting as a stem cell during normal homeostasis [8, 79-81]. In contrast, our study reveals the ongoing contribution to cell genesis from two parallel neural stem cell populations in the young adult hippocampus. These findings resonate with studies in epithelial tissues, such as mammary[82], prostate [83], and epidermis[84], which reveal a surprising degree of compartmentalization and homeostasis relying upon the parallel activity of seemingly lineage restricted stem cells. Different from epithelia, different population of RGLs in the adult dentate gyrus exhibit similar morphology, share certain common lineages and do not compartmentalize along spatial boundaries. Our study raised the question whether similar scenario occurs in other somatic tissues with adult stem cells.

Multiple evidences support the independence of different RGL neural stem cells, including Mash1 and MCM2 staining pattern (Figure 4A-C) and lack of switch of their stem cell properties over time under basal conditions (Figure 11). The distinct contribution of two stem cell populations under physiological conditions functionally enables cellular diversity alongside the robust production of a specific cell type. Ascl1$^{\#}$-RGLs, which repeatedly undergo asymmetric neurogenic self-renewing division, may act as the primary driver of constitutive neurogenesis. On the other hand, stochastic Nestin$^{\#}$-RGLs and Gli$^{\#}$-RGLs may contribute less frequently to basal tissue maintenance, but diversify cell genesis by creating new astroglia and additional RGLs. We rarely observed temporary spikes in neurogenesis within the Gli1$^{\#}$-RGL population or increases in astrogenesis within the Ascl1$^{\#}$-RGL population over the period examined (Figure 11), suggesting minimal conversion between these two populations under physiological conditions. After injury, however, neural stem cells that are normally stochastic in fate choice (Gli1$^{\#}$-RGLs and Nestin$^{\#}$-RGLs) become activated and appear to acutely adopt the behavior of neuronal fate biased stem cells (Ascl1$^{\#}$-RGLs). Interestingly, the increased generation of the neuronal lineage comes at the expense of gliogenesis. This conversion from multipotential to unipotential lineage bias is unexpected, considering that stem cells generally acquire greater lineage capacity after injury [20, 81, 82, 85]. We hypothesize that stochastic neural stem cells adapt their fate choices to meet the regenerative demand of the local niche – in this case, losing multipotentiality but gaining repetitive cycling ability to regenerate the neuronal lineage. Meanwhile upon injury, neurogenic Ascl1$^{\#}$-RGLs also differed in their injury response with increased symmetric self-renewal at the expense of asymmetric neurogenic cell division. One explanation for this behavior could be to replace loss of the majority of Ascl1$^{\#}$-RGLs during injury. Therefore, we revealed a complex homeostatic plasticity of different types of neural stem cells in the same region in response to injury.

Understanding stem cell behavior under physiological and injury conditions has implications for tissue plasticity and may ultimately guide future regenerative strategies. Here, we deconstruct neural stem cell complexity to reveal the contribution of two discrete stem cell populations to ongoing cell genesis in the young adult hippocampus, as well as their plasticity upon injury. Our study indicates that seemingly divergent stem cell phenotypes at the population level [24] can be attributed to specific subpopulations at the single-cell level, thereby providing a framework for establishing relationships among different stem cells as new states and populations become identified.

5 References

1. Blanpain, C. & Simons, B. D. Unravelling stem cell dynamics by lineage tracing. Nat Rev Mol Cell Biol 14, 489-502 (2013).
2. Gage, F. H. Mammalian neural stem cells. Science 287, 1433-8 (2000).
3. Goritz, C. & Frisen, J. Neural stem cells and neurogenesis in the adult. Cell Stem Cell 10, 657-9 (2012).
4. Temple, S. The development of neural stem cells. Nature 414, 112-7 (2001).
5. Weissman, I. L., Anderson, D. J. & Gage, F. Stem and progenitor cells: origins, phenotypes, lineage commitments, and transdifferentiations. Annu Rev Cell Dev Biol 17, 387-403 (2001).
6. Klein, A. M. & Simons, B. D. Universal patterns of stem cell fate in cycling adult tissues. Development 138, 3103-11 (2011).
7. Li, L. & Clevers, H. Coexistence of quiescent and active adult stem cells in mammals. Science 327, 542-5 (2010).
8. Mascre, G. et al. Distinct contribution of stem and progenitor cells to epidermal maintenance. Nature 489, 257-62 (2012).
9. Waddington, C. H. (London: Allen & Unwin, 1957).
10. Carlen, M. et al. Forebrain ependymal cells are Notch-dependent and generate neuroblasts and astrocytes after stroke. Nature neuroscience 12, 259-67 (2009).
11. Coskun, V. et al. CD133+ neural stem cells in the ependyma of mammalian postnatal forebrain. Proc Natl Acad Sci U S A 105, 1026-31 (2008).
12. Johansson, C. B. et al. Identification of a neural stem cell in the adult mammalian central nervous system. Cell 96, 25-34 (1999).
13. Blanpain, C. & Fuchs, E. Stem cell plasticity. Plasticity of epithelial stem cells in tissue regeneration. Science 344, 1242281 (2014).
14. Braun, T. & Martire, A. Cardiac stem cells: paradigm shift or broken promise? A view from developmental biology. Trends Biotechnol 25, 441-7 (2007).
15. Griffiths, M. J., Bonnet, D. & Janes, S. M. Stem cells of the alveolar epithelium. Lancet 366, 249-60 (2005).
16. Li, S., Sun, G., Murai, K., Ye, P. & Shi, Y. Characterization of TLX expression in neural stem cells and progenitor cells in adult brains. PLoS One 7, e43324 (2012).
17. Ming, G. L. & Song, H. Adult neurogenesis in the mammalian brain: significant answers and significant questions. Neuron 70, 687-702 (2011).
18. Muller-Sieburg, C. E., Sieburg, H. B., Bernitz, J. M. & Cattarossi, G. Stem cell heterogeneity: implications for aging and regenerative medicine. Blood 119, 3900-7 (2012).
19. Solanas, G. & Benitah, S. A. Regenerating the skin: a task for the heterogeneous stem cell pool and surrounding niche. Nat Rev Mol Cell Biol 14, 737-48 (2013).
20. Buczacki, S. J. et al. Intestinal label-retaining cells are secretory precursors expressing Lgr5. Nature 495, 65-9 (2013).
21. Ema, H., Morita, Y. & Suda, T. Heterogeneity and hierarchy of hematopoietic stem cells. Exp Hematol (2013).
22. Bonaguidi, M. A., Song, J., Ming, G. L. & Song, H. A unifying hypothesis on mammalian neural stem cell properties in the adult hippocampus. Curr Opin Neurobiol 22, 754-61 (2012).
23. Bonaguidi, M. A. et al. In vivo clonal analysis reveals self-renewing and multipotent adult neural stem cell characteristics. Cell 145, 1142-55 (2011).
24. Encinas, J. M. et al. Division-coupled astrocytic differentiation and age-related depletion of neural stem cells in the adult hippocampus. Cell Stem Cell 8, 566-79 (2011).
25. Steiner, B. et al. Differential regulation of gliogenesis in the context of adult hippocampal neurogenesis in mice. Glia 46, 41-52 (2004).
26. Sierra, A. et al. Microglia shape adult hippocampal neurogenesis through apoptosis-coupled phagocytosis. Cell Stem Cell 7, 483-95 (2010).
27. Ma, D. K., Bonaguidi, M. A., Ming, G. L. & Song, H. Adult neural stem cells in the mammalian central nervous system. Cell Res 19, 672-82 (2009).
28. Gabay, L., Lowell, S., Rubin, L. L. & Anderson, D. J. Deregulation of dorsoventral patterning by FGF confers trilineage differentiation capacity on CNS stem cells in vitro. Neuron 40, 485-99 (2003).
29. Kondo, T. & Raff, M. Oligodendrocyte precursor cells reprogrammed to become multipotential CNS stem cells. Science 289, 1754-7 (2000).
30. Palmer, T. D., Markakis, E. A., Willhoite, A. R., Safar, F. & Gage, F. H. Fibroblast growth factor-2 activates a latent neurogenic program in neural stem cells from diverse regions of the adult CNS. J Neurosci 19, 8487-97 (1999).
31. Suh, H. et al. In vivo fate analysis reveals the multipotent and self-renewal capacities of Sox2+ neural stem cells in the adult hippocampus. Cell Stem Cell 1, 515-28 (2007).
32. Kretzschmar, K. & Watt, F. M. Lineage tracing. Cell 148, 33-45 (2012).
33. Calzolari, F. et al. Fast clonal expansion and limited neural stem cell self-renewal in the adult subependymal zone. Nat Neurosci (2015).
34. Ihrie, R. A. & Alvarez-Buylla, A. Lake-front property: a unique germinal niche by the lateral ventricles of the adult brain. Neuron 70, 674-86 (2011).
35. Tsai, H. H. et al. Regional astrocyte allocation regulates CNS synaptogenesis and repair. Science 337, 358-62 (2012).
36. Ortega, F. et al. Oligodendrogliogenic and neurogenic adult subependymal zone neural stem cells constitute distinct lineages and exhibit differential responsiveness to Wnt signalling. Nat Cell Biol 15, 602-13 (2013).
37. Dranovsky, A. et al. Experience dictates stem cell fate in the adult hippocampus. Neuron 70, 908-23 (2011).

38. **DeCarolis, N. A. et al. In vivo contribution of nestin- and GLAST-lineage cells to adult hippocampal neurogenesis. Hippocampus 23, 708-19 (2013).**
39. **Jinno, S. Topographic differences in adult neurogenesis in the mouse hippocampus: a stereology-based study using endogenous markers. Hippocampus 21, 467-80 (2011).**
40. **Piatti, V. C. et al. The timing for neuronal maturation in the adult hippocampus is modulated by local network activity. J Neurosci 31, 7715-28 (2011).**
41. **Snyder, J. S., Ferrante, S. C. & Cameron, H. A. Late maturation of adult-born neurons in the temporal dentate gyrus. PLoS One 7, e48757 (2012).**
42. **Tashiro, A., Makino, H. & Gage, F. H. Experience-specific functional modification of the dentate gyrus through adult neurogenesis: a critical period during an immature stage. J Neurosci 27, 3252-9 (2007).**
43. **Ahn, S. & Joyner, A. L. In vivo analysis of quiescent adult neural stem cells responding to Sonic hedgehog. Nature 437, 894-7 (2005).**
44. **Kim, E. J., Ables, J. L., Dickel, L. K., Eisch, A. J. & Johnson, J. E. Ascl1 (Mash1) defines cells with long-term neurogenic potential in subgranular and subventricular zones in adult mouse brain. PLoS One 6, e18472 (2011).**
45. **Balordi, F. & Fishell, G. Mosaic removal of hedgehog signaling in the adult SVZ reveals that the residual wild-type stem cells have a limited capacity for self-renewal. J Neurosci 27, 14248-59 (2007).**
46. **Novak, A., Guo, C., Yang, W., Nagy, A. & Lobe, C. G. Z/EG, a double reporter mouse line that expresses enhanced green fluorescent protein upon Cre-mediated excision. Genesis 28, 147-55 (2000).**
47. **Lemberger, T. et al. Expression of Cre recombinase in dopaminoceptive neurons. BMC Neurosci 8, 4 (2007).**
48. **Muzumdar, M. D., Tasic, B., Miyamichi, K., Li, L. & Luo, L. A global double-fluorescent Cre reporter mouse. Genesis 45, 593-605 (2007).**
49. **Ge, S. et al. GABA regulates synaptic integration of newly generated neurons in the adult brain. Nature 439, 589-93 (2006).**
50. **Song, J. et al. Neuronal circuitry mechanism regulating adult quiescent neural stem-cell fate decision. Nature 489, 150-4 (2012).**
51. **Sun, G. J. et al. Seamless reconstruction of intact adult-born neurons by serial end-block imaging reveals complex axonal guidance and development in the adult hippocampus. J Neurosci 33, 11400-11 (2013).**
52. **Zhao, C., Teng, E. M., Summers, R. G., Jr., Ming, G. L. & Gage, F. H. Distinct morphological stages of dentate granule neuron maturation in the adult mouse hippocampus. J Neurosci 26, 3-11 (2006).**
53. **Hayes, N. L. & Nowakowski, R. S. Dynamics of cell proliferation in the adult dentate gyrus of two inbred strains of mice. Brain Res Dev Brain Res 134, 77-85 (2002).**
54. **Hodge, R. D. et al. Intermediate progenitors in adult hippocampal neurogenesis: Tbr2 expression and coordinate regulation of neuronal output. J Neurosci 28, 3707-17 (2008).**
55. **Zhao, C., Deng, W. & Gage, F. H. Mechanisms and functional implications of adult neurogenesis. Cell 132, 645-60 (2008).**
56. **Song, J. et al. Parvalbumin interneurons mediate neuronal circuitry-neurogenesis coupling in the adult hippocampus. Nat Neurosci 16, 1728-30 (2013).**
57. **Clayton, E. et al. A single type of progenitor cell maintains normal epidermis. Nature 446, 185-9 (2007).**
58. **Srinivas, S. et al. Cre reporter strains produced by targeted insertion of EYFP and ECFP into the ROSA26 locus. BMC Dev Biol 1, 4 (2001).**
59. **Andersen, J. et al. A transcriptional mechanism integrating inputs from extracellular signals to activate hippocampal stem cells. Neuron 83, 1085-97 (2014).**
60. **Weissman, I. L., Anderson, D. J. & Gage, F. H. Stem and progenitor cells: origins, phenotypes, lineage commitments, and transdifferentiations. Annu Rev Cell Dev Biol 17, 387-403 (2001).**
61. **Doetsch, F., Caille, I., Lim, D. A., Garcia-Verdugo, J. M. & Alvarez-Buylla, A. Subventricular zone astrocytes are neural stem cells in the adult mammalian brain. Cell 97, 703-16 (1999).**
62. **Basak, O., Giachino, C., Fiorini, E., Macdonald, H. R. & Taylor, V. Neurogenic subventricular zone stem/progenitor cells are Notch1-dependent in their active but not quiescent state. J Neurosci 32, 5654-66 (2012).**
63. **Fleming, W. H. et al. Functional heterogeneity is associated with the cell cycle status of murine hematopoietic stem cells. J Cell Biol 122, 897-902 (1993).**
64. **Imayoshi, I., Sakamoto, M., Yamaguchi, M., Mori, K. & Kageyama, R. Essential roles of Notch signaling in maintenance of neural stem cells in developing and adult brains. J Neurosci 30, 3489-98 (2010).**
65. **Kalmar, T. et al. Regulated fluctuations in nanog expression mediate cell fate decisions in embryonic stem cells. PLoS Biol 7, e1000149 (2009).**
66. **Altschuler, S. J. & Wu, L. F. Cellular heterogeneity: do differences make a difference? Cell 141, 559-63 (2010).**
67. **Chang, C. Y. et al. NFIB is a governor of epithelial-melanocyte stem cell behaviour in a shared niche. Nature 495, 98-102 (2013).**
68. **Ritsma, L. et al. Intestinal crypt homeostasis revealed at single-stem-cell level by in vivo live imaging. Nature 507, 362-5 (2014).**
69. **Levy, V., Lindon, C., Harfe, B. D. & Morgan, B. A. Distinct stem cell populations regenerate the follicle and interfollicular epidermis. Dev Cell 9, 855-61 (2005).**
70. **Nishimura, E. K. et al. Dominant role of the niche in melanocyte stem-cell fate determination. Nature 416, 854-60 (2002).**
71. **Tumbar, T. et al. Defining the epithelial stem cell niche in skin. Science 303, 359-63 (2004).**
72. **Codega, P. et al. Prospective identification and purification of quiescent adult neural stem cells from their in vivo niche. Neuron 82, 545-59 (2014).**
73. **Merkle, F. T., Mirzadeh, Z. & Alvarez-Buylla, A. Mosaic organization of neural stem cells in the adult brain. Science 317, 381-4 (2007).**
74. **Mich, J. K. et al. Prospective identification of functionally distinct stem cells and neurosphere-initiating cells in adult mouse forebrain. Elife 3, e02669 (2014).**

75. **van der Wath, R. C., Wilson, A., Laurenti, E., Trumpp, A. & Lio, P. Estimating dormant and active hematopoietic stem cell kinetics through extensive modeling of bromodeoxyuridine label-retaining cell dynamics. PLoS One 4, e6972 (2009).**
76. **Rocheteau, P., Gayraud-Morel, B., Siegl-Cachedenier, I., Blasco, M. A. & Tajbakhsh, S. A subpopulation of adult skeletal muscle stem cells retains all template DNA strands after cell division. Cell 148, 112-25 (2012).**
77. **Rompolas, P., Mesa, K. R. & Greco, V. Spatial organization within a niche as a determinant of stem-cell fate. Nature 502, 513-8 (2013).**
78. **Hara, K. et al. Mouse spermatogenic stem cells continually interconvert between equipotent singly isolated and syncytial states. Cell Stem Cell 14, 658-72 (2014).**
79. **Collins, C. A., Zammit, P. S., Ruiz, A. P., Morgan, J. E. & Partridge, T. A. A population of myogenic stem cells that survives skeletal muscle aging. Stem Cells 25, 885-94 (2007).**
80. **Leung, C. T., Coulombe, P. A. & Reed, R. R. Contribution of olfactory neural stem cells to tissue maintenance and regeneration. Nat Neurosci 10, 720-6 (2007).**
81. **Stange, D. E. et al. Differentiated Troy+ chief cells act as reserve stem cells to generate all lineages of the stomach epithelium. Cell 155, 357-68 (2013).**
82. **Van Keymeulen, A. & Blanpain, C. Tracing epithelial stem cells during development, homeostasis, and repair. J Cell Biol 197, 575-84 (2012).**
83. **Ousset, M. et al. Multipotent and unipotent progenitors contribute to prostate postnatal development. Nat Cell Biol 14, 1131-8 (2012).**
84. **Page, M. E., Lombard, P., Ng, F., Gottgens, B. & Jensen, K. B. The epidermis comprises autonomous compartments maintained by distinct stem cell populations. Cell Stem Cell 13, 471-82 (2013).**
85. **Haug, J. S. et al. N-cadherin expression level distinguishes reserved versus primed states of hematopoietic stem cells. Cell Stem Cell 2, 367-79 (2008).**

Curriculum Vitae

Ryan P. Stadel

Department of Human Genetics	
Institute for Genetic Medicine	Tel: (409) 718-1269
Johns Hopkins University	
733 N. Broadway / MRB 706 Baltimore, MD 21205 USA	CITIZENSHIP: US
E-mail: rstadel1@jhmi.edu	DOB: 5/6/1982 Hinsdale, IL

Education

2000-2004	Texas A&M University	B.S. Biomedical Science
2009-Present	Johns Hopkins School of Medicine	Ph.D. Candidate Human Genetics

Research

2009-present *Graduate Student,* Department of Human Genetics. Johns Hopkins University School of Medicine, Baltimore, MD. Advisor: Dr. Hongjun Song

Thesis: In vivo clonal analysis of adult neural stem cells

2008-2009 *Research Assistant*, Department of Orthopaedic Surgery. Johns Hopkins University, Baltimore, MD. Advisors: Drs. Kristy Weber and Scott Kominsky

Research: Investigate Enpp1 in bone metastasis

2006-2008 *Histocompatability Technologist II*, Histocompatibility and

Transplant Laboratory. Medstar Research Institute, Hyattsville, MD. Advisor: Dr. William Ward

Clinical: Laboratory HLA testing and organ transplant matching

2004-2006 *Research assistant*, HLA Laboratory. University of Texas Health Science, Houston, TX. Advisor: Dr. Ronald H. Kerman

Clinical: Laboratory HLA testing and organ transplant matching

2003-2004 *Undergraduate Researcher,* Department of Biochemistry and Biophysics. Texas A&M University, College Station, TX. Advisor: Dr. James C. Hu

Research: Investigate LTTR protein to protein interactions in *E. coli*

Awards, Scholarships, and Honors

2013 Keystone Neurogenesis 2013: National Institute of Neurological Disorders and Stroke (NINDS)/National Institute on Aging (NIA) Scholarship

2004 Texas A&M University B.S. in Biomedical Science graduate Cum Laude

Publications

Refereed Articles

1. Bonaguidi MA*, **Stadel RP*,** Krieger T, Berg D, Sun GJ, Namgung Y, Park JY, Park S, Oh JJ, Ming GL, Simons BD, Song H. Different states and discrete populations of neural stem cells in the adult hippocampus. *In preparation.*

2. Sun GJ*, Zhou Y*, **Stadel RP*,** Moss J, Yong JHA, Randall RR, Toni N, Song H, Ming GL. Tangential migration of neuroblasts for glutamatergic neurons in the adult brain. *In preparation.*

3. Lau WM, Doucet M, **Stadel R**, Huang D, Weber KL, Kominsky SL (2013) Enpp1: a potential facilitator of breast cancer bone metastasis. *PLoS One.* Jul 5;8(7).

4. Bonaguidi MA, Wheeler MA, Shapiro JS, **Stadel RP**, Sun GJ, Ming GL, Song H (2011) In vivo clonal analysis reveals self-renewing and multipotent adult neural stem cell characteristics. *Cell* 145(7):1142-55.

*equal contribution

Reviews & Book Chapter

Bonaguidi MA, **Stadel RP,** Sun J, Ming GL, Song H. Diversity of Neural Precursors in the Adult Mammalian Brain. CSH Perspectives. *In press.*

Invited Lecturer

2013-1 Coexistence of quiescent and active radial neural stem cell populations in the adult hippocampus. Keystone Symposia: Adult Neurogenesis (A5), 2013. Taos, NM USA.

2013-2 Dynamics of stem cell niche biology in vivo: coexistence of quiescent and active radial neural stem cells in the adult hippocampus. The Center for Cell Dynamics & The Developmental Biology Research Group: Jan. 11. 2013. JHMI.

Abstracts from Meetings

1. **Stadel RP**, Bonaguidi MA, Krieger T, Sun GJ, Berg DA, Namgung Y, Park JY, Park S, Oh JJ, Reed RR, Ming GL, Simons BD, Song H. Clonal lineage tracing of mash1# radial precursor cells in the adult mouse dentate gyrus reveals neural stem cell characteristics. Annual Meeting. Society for Neuroscience: (607.25/A25), 2013.
2. **Stadel RP**, Bonaguidi MA, Park S, Namgung Y, Jin Oh J, Reed R, Simons B, Song H, Ming GL. Coexistence of Quiescent and Active Radial Neural Stem Cell Populations in the Adult Hippocampus. Keystone Symposia: Neurogenesis (J7), 2013.
3. **Stadel RP**, Bonaguidi MA, Sun GJ, Randall RR, Ming GL, Song H. In vivo clonal analysis of intermediate progenitor cells in the adult mouse hippocampus. Annual Meeting. Society for Neuroscience: (30.11/A33), 2011.
4. Bonaguidi MA, Wheeler M, Shapiro JS, **Stadel R**, Sun GJ, Ming GL and Song H. Clonal analysis of radial glia-like cells reveals self-renewal and multipotential properties in the adult hippocampus. Keystone Symposia: Adult Neurogenesis (A5), 2011.
5. Shapiro JS, Bonaguidi MA, Wheeler M, Sun GJ, **Stadel RP**, Ming GL, Song H. Heterogeneous neural stem cell characteristics in the adult hippocampus revealed by in vivo clonal analysis. Annual Meeting.Society for Neur0science: (31.27/D6), 2010.

6. Bonaguidi MA, **Stadel RP**, Chiang J, Quinones–Hinojosa A, Ming GL, and Song H. Human neural stem cells from temporal lobe biopsies and pluripotent stem cells. Maryland Stem Cell Research Foundation Symposium, 2010.

Teaching

2013	*Teaching Assistant.* ME:440.815 Stem Cells.
2009-2012	*Mentor.* Incentive Mentoring Program, Baltimore MD. Mentoring at risk inner city High School youth tutoring them throughout high school and advising a student through his first year of college.
2008-2009	*Advisor*. Orthopaedics, Johns Hopkins University, Balitmore MD. Mentoring medical student during a summer research rotation.

Professional Societies

2013-2014	International Society of Stem Cell Researchers (ISSCR)
2006-2008	Certified Histocompatibility Technologist (CHT), American Society for Histocampatability and Immunogenetics (ABHI)